

**ULTRA-WIDEBAND RF PHOTONIC
PHASED ARRAY ANTENNA**

by

Dylan D. Ross

A thesis submitted to the Faculty of the University of Delaware in partial fulfillment of the requirements for the degree of Master of Science in Electrical and Computer Engineering

Spring 2016

© 2016 Dylan D. Ross
All Rights Reserved

ProQuest Number: 10156532

All rights reserved

INFORMATION TO ALL USERS

The quality of this reproduction is dependent upon the quality of the copy submitted.

In the unlikely event that the author did not send a complete manuscript and there are missing pages, these will be noted. Also, if material had to be removed, a note will indicate the deletion.



ProQuest 10156532

Published by ProQuest LLC (2016). Copyright of the Dissertation is held by the Author.

All rights reserved.

This work is protected against unauthorized copying under Title 17, United States Code
Microform Edition © ProQuest LLC.

ProQuest LLC.
789 East Eisenhower Parkway
P.O. Box 1346
Ann Arbor, MI 48106 - 1346

**ULTRA-WIDEBAND RF PHOTONIC
PHASED ARRAY ANTENNA**

by

Dylan D. Ross

Approved: _____
Dennis W. Prather, Ph.D.
Professor in charge of thesis on behalf of the Advisory Committee

Approved: _____
Kenneth E. Barner, Ph.D.
Chair of the Department of Electrical and Computer Engineering

Approved: _____
Babatunde Ogunnaike, Ph.D.
Dean of the College of Engineering

Approved: _____
Ann L. Ardis, Ph.D.
Senior Vice Provost for Graduate and Professional Education

ACKNOWLEDGMENTS

Although this thesis primarily consists of efforts made in the past year, research lessons learned and experienced gained extend back to my sophomore year of undergraduate studies. Thus, I would like to take a moment to express my gratitude to all colleagues and mentors who have had an impact on me throughout this time.

First, I would like to thank my advisor, Dr. Dennis Prather, for all his support and guidance throughout my time in his lab. I entered his lab as a sophomore without a true appreciation of the RF photonics field and very little electrical engineering experience in general; nevertheless, he immediately provided encouragement and all the resources necessary to become, and grow as a researcher. His enthusiasm, motivation, and push to always take an extra step forward have afforded me a tremendous, gratifying opportunity in being part of the stimulating and challenging journey in attempt to push RF photonic technology passed current barriers.

I want to separately thank Drs. Benjamin Olbricht and David Eng, who both have been very valuable as mentors and in keeping the lab environment fun and interesting. From day one, Dave took time out of his schedule to teach me the basics of tackling research hurdles. I owe the majority of my knowledge on the subject to his patience and clarification anytime I was confused. Ben always encouraged me to exceed general expectations, pushing me to strive towards next-level goals, even when I didn't see them as possible. His openness to new ideas has helped me use creativity and unconventional ideas to help solve problems without fearing failure. As a colleague and friend, his advice has always been exceptionally valuable.

I owe an unmeasurable amount of thanks to Dr. Shouyuan Shi. His gift of patience and profound aptitude to transfer complex concepts into simple, clear

explanations are unmatched. I am extremely grateful to have had the opportunity to have him as a mentor for the work presented in this thesis. Additionally, I would like to thank my partner in this work, Matthew Konkol. His ability to meticulously analyze individual components and pieces of the bigger picture, as well as pass on his vast knowledge of photodiode operation and optical fiber communications has played a large role in the successes of this research. Furthermore, the shared capability to find humor within the challenges endured throughout this work has made the process much more enjoyable. I want to also thank Charles Harrity and Andrew Wright for their help, without their willingness to aid in certain processes, this work would not be possible.

It goes without saying that this experience was also positively impacted by all of the graduate students and researchers associated with Dr. Prather's research. I thank everyone who I had a chance to meet and work with throughout my 5 years of working in the group. Each person has contributed to an enjoyable, friendly work environment that is much appreciated.

Finally, I would like to thank my family and friends for all of their support along the way. Most importantly, my parents, Ann and Duane, who always inspire and support me in everything I do, allow me to grow as my own person, and are there any time I am going through tough times. Secondly, I would like to thank my friends, Sam Modlin and Stephen Herbein, for helping me maintain a work-life balance and providing insight on all my frustrations. Last, but not least, I am overly grateful for my girlfriend, Logan, for her continual encouragement throughout lows of the process, and celebration of each accomplishment, no matter how small.

TABLE OF CONTENTS

LIST OF TABLES	vii
LIST OF FIGURES	viii
ABSTRACT	xii

Chapter

1	INTRODUCTION	1
1.1	Ultra-Wideband (UWB) Phased Array Antennas	1
1.2	Microwave Photonics	4
1.3	Overview	6
2	CONNECTED ARRAY ANTENNA.....	8
2.1	Introduction to Connected and Tightly-Coupled Array Antennas	8
2.2	Circuit Model Representation.....	12
2.3	Electrical Excitation	14
2.3.1	Unbalanced Feeding	15
2.3.2	Balanced Feeding	18
3	OPTICAL FEEDING PHASED ARRAY ANTENNAS	20
3.1	Modified Uni-Traveling Carrier Photodiodes	21
3.2	Ultra-Wideband Feed Network for Photonic Phased Arrays	23
3.2.1	UWB Tunable Photonic RF Signal Generation.....	23
3.2.2	Phase Control Network.....	25
3.3	Conclusion.....	29
4	PHOTODIODE-COUPLED ANTENNA DESIGN AND MODELING.....	30
4.1	Photodiode-Coupled Antenna Model	30
4.1.1	Connected Array Model	30
4.1.2	Coupling Photodiode to CA Antenna.....	32

4.2	Infinite Photodiode-Coupled Array Antenna Modeling.....	36
4.2.1	HFSS Full-Wave Electromagnetic Modeling Studies.....	37
4.2.1.1	Substrate	37
4.2.1.2	Bias Line Circuitry	39
4.2.1.3	Optical Alignment Components	42
4.2.1.4	Inductive Peaking	46
4.2.2	Beam Steering	47
4.3	Discrete Photodiode-Coupled Array Antenna Modeling	49
5	FABRICATION AND OPTICAL INTEGRATION.....	54
5.1	Antenna.....	56
5.2	Photodiode Integration	59
5.3	Coupling Photodiodes to Optical Feed Network.....	62
5.3.1	Spacer/Mount Preparation	63
5.3.2	GRIN Lens/Mating Sleeve Unit Preparation.....	64
5.3.3	Optical Alignment	64
5.4	Packaging	68
6	TX SYSTEM CHARACTERIZATION.....	70
6.1	System Architecture	70
6.2	Characterization and Results	74
7	CONCLUSION	78
7.1	Summary.....	78
7.2	Future Work.....	78
	REFERENCES.....	81

LIST OF TABLES

Table 5.1: Comparison of photodiode responsivity before and after optical alignment.....	66
--	----

LIST OF FIGURES

Figure 1.1:	Overview of UWB antenna elemental radiator categories.	2
Figure 1.2:	Simple microwave photonic link with E/O conversion and O/E conversion.	5
Figure 2.1:	Uniform current sheet of current density \mathbf{J} , phase shifting of the current density results in radiation beam steering in the (θ, ϕ) direction [42].	9
Figure 2.2:	Conceptual CSA of adjacent connected-dipole arrays (left) with dipole spatial periods dx and dy , and it's equivalent circuit model (right).	10
Figure 2.3:	Equivalent circuit model for TCA of dipoles positioned above a PEC. ..	12
Figure 2.4:	(a) Example connected array dipole antenna. (b) HFSS full wave simulation and circuit model comparison of CA dipole antenna.	13
Figure 2.5:	Feed organizer used to route coaxial feed to dual-polarization CSA antenna, from [9] [26].	16
Figure 2.6:	Common-, TE ₁₀ - mode resonance introduced by unbalanced feeding (solid arrows mimic current flow, dotted lines depict electric field associated with common-mode resonance.	17
Figure 2.7:	(a) External balun linking 50Ω CPW electrical feed and 200Ω CPS of dipole TCA [29], (b) schematic of 50Ω CPW/coaxial cable connection [29], (c) UWB balun with microstrip-stripline transition [33], and (d) Hybrid integrated balun [27].	19
Figure 3.1:	28 μm diameter MUTC photodiode fabricated at University of Delaware.	22
Figure 3.2:	(a) Bandwidth performance of 28 μm diameter photodiode, and (b) power output of approximately 24.8 dBm at 25 GHz.	22
Figure 3.3:	Schematic of photonic radiofrequency signal generation system [21]. Image courtesy of Dr. Garrett J. Schneider.	24

Figure 3.4: UWB phase control optical feed network [20]. Image courtesy of Dr. Shouyuan Shi.....	25
Figure 4.1: Simulation model of infinite hybrid bow tie/dipole antenna where $L_f = 0.15$ mm, $L_t = 1.5$ mm, $L_d = 1.6$ mm, $W_f = 0.1$ mm, and $W_d = 3.0$ mm.....	31
Figure 4.2: Simulated active resistance and reactance results of infinite CA.	32
Figure 4.3: Equivalent circuit representation of photodiode-coupled CA antenna.	33
Figure 4.4: Simulated aluminum nitride substrate effect on active radiation impedance and total radiate power at 70 mA photocurrent.....	38
Figure 4.5: Bias line network for photodiode-coupled CA antenna, $g/2$ is the capacitive coupling gap between dipole edges, s_b is the spacing of the bias line from the edge of the dipole, and w_b is the bias line width.	40
Figure 4.6: (a) Surface current distributions at working 15 GHz and resonant 23 GHz, (b) active impedance response to s_b sweep, solid lines represent resistance and dotted represent reactance, and (c) total radiate power. ..	41
Figure 4.7: Initial proposed optical feed integration technique for CA antenna.	43
Figure 4.8: Spacer/mount body designs made out of ABS, a common 3D printed material, to reduce dielectric effects.....	44
Figure 4.9: Simulated spacer/mount effects on active radiation impedance and total radiate power at 70 mA photocurrent.....	45
Figure 4.10: Inductive peaking RF current feed, R is the radius of the circles.	46
Figure 4.11: Effects of inductive peaking on active impedance, solid lines represent resistance and dotted represent reactance, and total radiate power at 70 mA photocurrent.....	47
Figure 4.12: Simulated CA beam steering results at 70 mA photocurrent. The left graph shows the bandwidth of an infinite array, while the right shows the radiation pattern at different scan angles for a 12 GHz working frequency [44].	48
Figure 4.13: (a) 1 x 4 photodiode-coupled CA antenna with optical integration components, and (b) boundary conditions applied for finite modeling. .	50

Figure 4.14: Surface current distribution for discrete 1 x 4 photodiode CA antenna model at (a) 5 GHz without flanking resistors (FR), (b) 5 GHz with surrounding FR, (c) 12 GHz w/o, (d) 12 GHz w/ FR, (e) 15 GHz w/o FR, and (f) 15 GHz w/ FR.	52
Figure 4.15: Active impedance and total radiated power of 1 x 4 CA antenna.....	53
Figure 5.1: Overview of 1 x 4 photodiode-coupled CA antenna with integration of optical components linked to feed network.....	55
Figure 5.2: Pressure-driven filtering apparatus used for NR2-8000P filtration.	57
Figure 5.3: Fabricated CA antenna with biasing feed network connection port, 5 μ m DC bias-block gap (top right), and photodiode bond pads (bottom right).	59
Figure 5.4: Post-disconnection photodiode bond pad with resultant indentations.	60
Figure 5.5: Four photodiodes thermally and electrically connected to CA antenna. .	61
Figure 5.6: Bias control board used for DC reverse-bias supply to photodiodes, and as a current link for reading optical alignment currents.	62
Figure 5.7: (a) Schematic of GRIN lens/sleeve/fiber unit set on spacer/mount ledge and (b) 3D printed fiber spacer/mount used for 1 x 4 CA antenna.....	63
Figure 5.8: Optical integration set-up during alignment of fourth element.	65
Figure 5.9: Successful integration of 4 single-mode optical fibers to MUTC photodiode-coupled CA antenna [44].	67
Figure 5.10: Packaged photodiode-coupled CA antenna with mounted biasing board.....	69
Figure 6.1: Tx system architecture including UWB tunable photonic RF source, phase control network, CA antenna, and data analysis and control equipment.	70
Figure 6.2: Tunable photonic RF source installed into a rack mount [42].....	71
Figure 6.3: Optical phase control network assembled in rack mount [42].....	73
Figure 6.4: 1x4 active element CA antenna radiating into the fair-field to a horn receive antenna connected to an ESA by a 2.4 mm RF cable.	74

Figure 6.5: Effective radiate power demonstrated by 1 x 3 photodiode-coupled CA antenna at (a) 60 mA and (b) 90 mA..... 76

Figure 6.6: Time-stamped plot of two periods of -90° to +90° beam steering at an operating frequency 15 GHz for (a) 60 mA photocurrent operation and (b) 90 mA photocurrent operation. The troughs represent -90° and +90° directions and peaks represent broadside displaying an extinction ratio of 34 dBm at 60 mA and 19 dBm at 90 mA. 77

Figure 7.1: Proposed low-profile 1 x 8 photodiode-coupled CA antenna design. 79

ABSTRACT

Modern RF antenna systems are being asked to address many simultaneous and pressing challenges, e.g., wide operational bandwidth, dynamic gain profiles, and conformal profiles. One way to address these is to develop a flexible and ultra-wideband (UWB) phased array antenna. However, the design, fabrication, and integration of such an array using an all-RF feed is exceedingly difficult. Thus, presented is an optical feeding technique to achieve efficient excitation of an UWB connected-array (CA) antenna. By feeding the array optically, preservation of the theoretical bandwidth and low-profile of elementary connected dipole elements is enabled. Coupling of light to a photodiode merely requires enough space to firmly secure a fiber ferrule, allowing population of more densely packed arrays, namely the CA, which offers potentially wide operational bandwidth. Additionally, optical feeding of the array can provide low noise excitation of the radiating elements, which supports high fidelity beam steering of independent signals over the array's ultra-wide bandwidth along with variable gain with suitable apodization. Currently all of these abilities are unattainable by conventional electronic feeding networks. Previously the main limiting factor for the realization of such an optical system was the low power handling capability of the photodiode at the antenna feed point. Recently, however, modified uni-travelling carrier (MUTC) photodiodes, flip-chip bonded to high-thermal conductivity aluminum nitride (AlN), have achieved output powers of over 1 W at 10 GHz under CW operation [37], and over 10 W using pulsed power modulation [38]. A robust prototype MUTC photodiode-integrated antenna array on AlN with direct fiber

feed to each antenna element is discussed and demonstrated that provides 5-20 GHz bandwidth and size, weight, and power (SWaP) superior to conventional electronic phased array systems [44].

Chapter 1

INTRODUCTION

Increased complexity and congestion of today's electromagnetic (EM) environment prompts unprecedented advancements in next generation communication systems to accommodate bandwidth and multi-functionality demands. Current avionic platforms commonly achieve all mission requirements through multiple narrowband RF devices conjoined into overly complicated, large, heavy, and costly systems. By replacing overabundant narrowband RF devices with fewer wideband active electronically scanned antennas (AESAs), a shift towards transcending future communication system demands is realized by accomplishing radar, passive electronic support, and active electronic countermeasures through a single broadband radio aperture.

Development of AESAs encompass several trends and requirements [1]: 1) multi-functionality, *i.e.*, supporting various applications through multiple radiating elements with polarization flexibility over independently steerable beams; 2) low profile configurations enabling structural efficiency and diminished EM signatures; 3) bandwidth extension towards operating frequencies into mm-wave regime to escape congested bands (<6GHz); 4) emphasis on size, weight, power, and cost (SWaP+C).

1.1 Ultra-Wideband (UWB) Phased Array Antennas

In recent decades, substantial efforts to satisfy these requirements through UWB array antennas have been demonstrated by tapered-slot antennas (TSAs) [2-4], bunny-ear antenna arrays [5-7], fragmented antennas [8], and tightly coupled arrays (TCA) [9, 10]. Elemental radiators formulating phased array antennas determine the

overall performance and characteristics of the array as a whole. Each elemental radiator provides a unique advantage displayed in Figure 1.1.

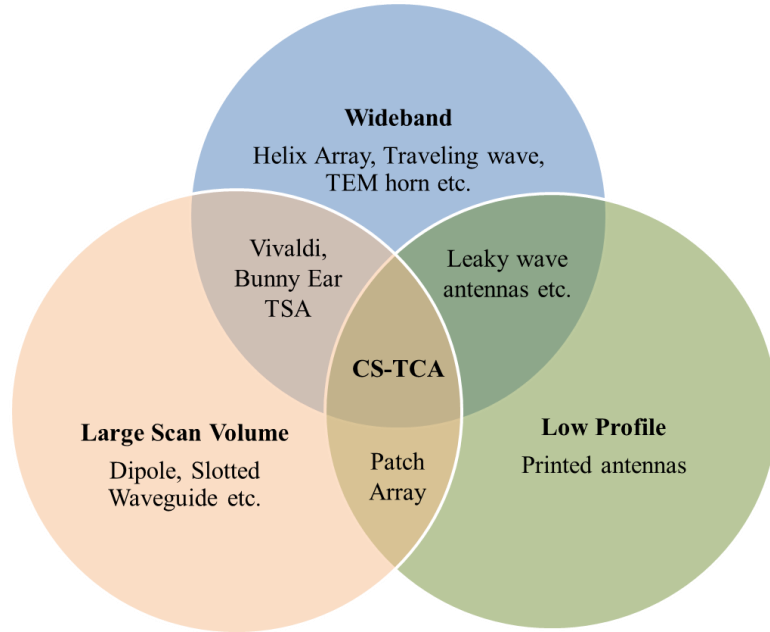


Figure 1.1: Overview of UWB antenna elemental radiator categories.

The first generation of these designs primarily consisted of TSAs and bunny-ear antenna arrays. TSAs typically provide a 3:1 bandwidth, however suffer from high profile, high-order resonance induced modes, and high cross-polarization in the E- and H- planes. Mitigation of profile and scan blindness while maintaining a comparable operational bandwidth can be achieved with the bunny-ear antenna. Unfortunately, the feeding system of a bunny-ear array requires baluns, *i.e.*, balanced to unbalanced transformers, for connection of coaxial cables to a parallel strip-line input for operation. Consequently, the operation bandwidth becomes constrained by balun functionality.

The second generation of UWB phased array designs employ connected dipoles and tightly coupled elements as radiating elements modeled after Wheeler's current sheet antenna (CSA) [11], a classical model to study connected array (CA) and TCA performance. Unlike the first generation designs, a dipole-based CSA design provides an inherent conformal, planar structure by fabricating dipole arrays onto thin substrates. Additionally, infinite dipole CSAs under constant phase exhibit a frequency independent radiation impedance of half free space plane wave impedance, $R_o = 188 \Omega$, due to bidirectional radiation yielding a theoretically infinite bandwidth. When the aperture current phase is shifted, the beam begins to steer away from the broadside resulting in TE and TM radiation modes with impedances of $R_o \cos\theta$ and $R_o/\cos\theta$, respectively, located in principle planes. Although the array impedance is a function of scan angle, a large tuning range remains attainable [12]. Additionally, contrary to other CSA designs including interleaved-spiral arrays or genetic algorithm created fragmented-antenna arrays, connected-dipole arrays experience low cross-polarization. Therefore, dipole-based CSA designs, *i.e.*, dipole CA and TCA antennas set an unmatched foundation for an UWB AESA frontend radiator.

As a pure radiating element the dipole CA and TCA antennas are far superior to other UWB AESA options; however, integration with an electronic phase feeding architecture introduces severely detrimental effects. At the core of performance degradation is the traditional 50Ω RF coaxial cable links which supply power to each array antenna element. Immediately implicit is a substantial impedance mismatch, $\sim 4:1$, between the half free space plane wave impedance of the CSA and the coax lines. Additionally, the dipole elements populating the array are symmetrical structures requiring balanced current feed distribution, *i.e.*, equal amplitude and

opposite phase in each dipole arm. This balanced feed requirement combined with the impedance mismatch require baluns for efficient excitation and impedance transformation, but at the cost of either decreased bandwidth, decreased operational frequency, scan blindness, or profile inadequacy. Even without a balun, structural and profile issues arise due to two cases; CSAs require placement of excitation feedlines perpendicular to the dipoles and migration towards the mm-wave regime is restricted by the dimensional requirements of proximal coax-dipole connection, particularly at high GHz frequencies. Based on these issues, effective electrical excitation of CSAs becomes the primary limitation to meeting AESA goals.

1.2 Microwave Photonics

Recent advances in microwave electronics corresponding to progressions in communication applications have drastically increased system complexity. Eventually these increases in application needs will push microwave electronics towards limitations in multiple areas. First, source tunable range of voltage controlled oscillators are restricted primarily to narrowband ranges. Next, data capacity controlled by Nyquist-Shannon sampling theorem shows data rates are set by carrier frequencies which is a primary bottleneck for microwave electronic communications. Lastly, these rapidly growing systems quickly exceed minimum SWaP requirements due to bulky, expensive RF cables yielding a substantial 360 dB/km propagation loss factor [13].

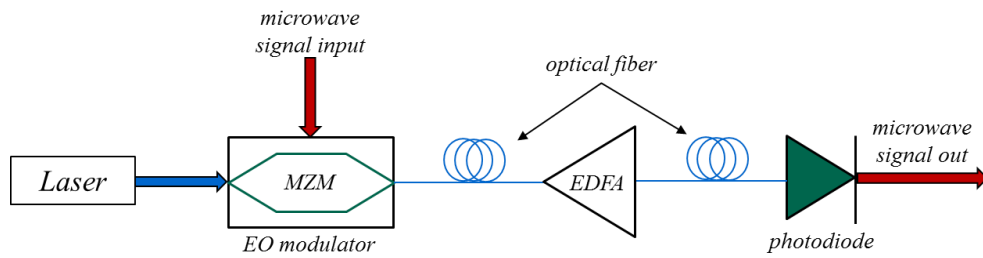


Figure 1.2: Simple microwave photonic link with E/O conversion and O/E conversion.

Lasers, low loss silica fibers, and low noise optical amplifiers promise capabilities of THz regime data transmission with propagation losses <0.5 dB/km, presenting a theoretically frequency independent platform for high-speed communications [14,15]. Lasers' bandwidth enabling tuning capabilities alone categorize photonics as a "natural fit" for high frequency/data rate applications with a common comparison of 1 nm tuning being equivalent to 125 GHz bandwidth at 1550 nm. Furthermore, optical fibers light weight and immunity to EMI aid in improving SWaP and efficiency in future systems. Additionally, leveraging these point-to-point advantages of optical fiber communications in conjunction with microwave frequency range atmospheric attenuation properties permits advancement of microwave systems without the same limitations previously mentioned. This interplay between optical and microwave frequency regimes is the basis of the rapidly growing microwave photonics discipline.

Microwave photonics technology performance is primarily limited by the conversion between optical and electrical domains; however, considerable advancements in recent years has afforded both high performance electrical to optical and optical to electrical conversion. Transducing between electrical to optical domains is accomplished through electro-optic (EO) modulators which are now capable of

ultra-broadband operation up to 300 GHz in traveling-wave lithium niobate (LiNbO_3) designs [16]. State of the art photodiodes exhibit similarly impressive performance metrics for broadband optical to electrical conversion, allowing for high frequency, high gain, low noise figure, and high linearity photonic links [17-19].

Implementation of this existing technology affords momentous possibilities for UWB AESA technology. By pairing a CSA with a photonic network rather than microwave electronic feeds, realizable advances towards matching AESA trends and requirements becomes possible. The array of CA of dipoles can be directly integrated with MUTC photodiodes, designed at the University of Virginia and fabricated at the University of Delaware, for transmit (Tx) excitation. Feeding these high-power, high-linearity photodiodes is an optical phase feed network [20] backed by an injection-seeding based source capable of providing signals from 0.5 to 110 GHz with a linewidth <1 Hz and ultra-low phase noise [21]. This proposed photonically driven UWB phased array antenna design offers considerable advantages over traditional systems in areas such as extreme power efficiency, information capacity, frequency agility, and spatial beam diversity.

1.3 Overview

The focus of this research is demonstrating wide scan angle beam steering capabilities over an UWB with an optically excited CA antenna. The starting point will be CSA theory, which will be discussed in depth and paired with a review of previous electrically addressed CSA-based designs in Chapter 2. Next, in Chapter 3 an alternative photonics-based excitation technique is presented; a two-tone optical signal generated by an UWB tunable photonic RF source will be coupled through an optical phase feed network for photomixing on MUTC photodiodes directly integrated onto a

CSA antenna. From here, the core of the research is illustrated in Chapter 4. A photodiode-coupled antenna model is developed by connecting a CSA theory-matched CA dipole antenna with a mathematical model of the MUTC photodiodes. A 1 x 4 photodiode-coupled CA antenna is then optimized using full-wave electromagnetic simulation software to satisfy requirements of wide-scanning angle performance over a 4:1 bandwidth. Chapter 5 covers the transfer of the computational antenna model through the fabrication and integration of the photodiodes and optical feeding components. Lastly, Chapter 6 includes Tx system prototype architecture and characterization followed by a reflection on this research and a future direction of the system in Chapter 7.

Chapter 2

CONNECTED ARRAY ANTENNA

2.1 Introduction to Connected and Tightly-Coupled Array Antennas

For modern RF antenna systems, it is desired to develop an UWB, low-profile antenna functioning as a single, wide-scanning aperture. Traditional phased array antennas employ weakly coupled elements, acting as independently isolated elements in the near-field with superposition contribution to the arrays far-field radiation pattern. At higher frequencies, these weakly coupled arrays endure bandwidth degradation due to grating lobes. In an effort to prevent these grating lobes, elemental radiator spacing can be reduced; however, this introduces detrimental mutual coupling at lower frequencies. Thus, traditional weakly coupled arrays are generally designed with narrowband application specific bandwidth requirements.

In an effort to improve phased array antenna performance, Wheeler systematically studied electronically scanned arrays via infinite array models [11]. Wheeler proposed in 1965 that an infinite array, shown in Figure 2.1, formulated as a uniform sheet of current J with constant phase will produce identical bidirectional broadside radiation of two TEM-mode plane waves across all frequencies. By phasing the lines of current, the broadside radiation can be steered in two principle planes, i.e., the x,z and y,z planes.

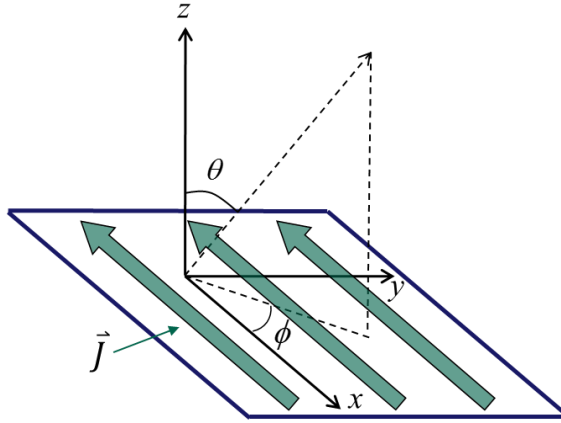


Figure 2.1: Uniform current sheet of current density \mathbf{J} , phase shifting of the current density results in radiation beam steering in the (θ, ϕ) direction [42].

This current sheet array (CSA) was viewed by Wheeler as the limit of closely spaced dipole elements popularly used for their low cross-polarization and profile properties. Modeling of dipoles into the CSA concept was initially accomplished through infinite parallel plate waveguides with PEC walls defining the dipole array unit cells' boundaries. The impedance of these waveguides was determined to be equal to the ratio of the waveguides height over the cross-sectional area multiplied by the intrinsic impedance of free-space [22]. By designing equivalent square unit cells and factoring in the CSA's inherent bidirectional radiation, the broadside radiation impedance becomes half of the plane-wave impedance of free space ($R_o = 188 \Omega$). As the current is phased, the radiation impedance of the TE- and TM- modes become $R_o \cos\theta$ and $R_o / \cos\theta$, respectively, resulting in an antenna impedance proportional to the beam direction and not operational frequency, *i.e.*, a theoretically infinite relative bandwidth [11]. This scan angle dependent impedance can be interpreted as the

waveguide cross-sectional area being reduced as the beam is directed away from broadside.

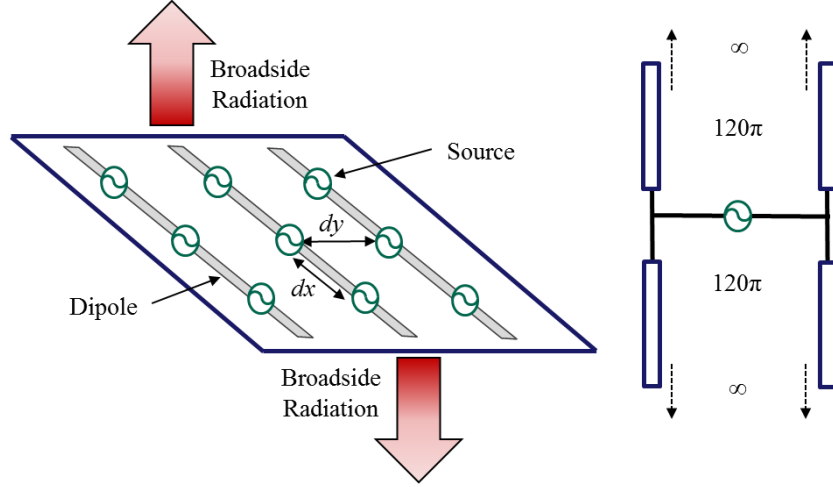


Figure 2.2: Conceptual CSA of adjacent connected-dipole arrays (left) with dipole spatial periods dx and dy , and its equivalent circuit model (right).

Conceptually, a CSA can be realized by populating an array of equally spaced adjacent infinitely-connected dipole elements, referred to as a connected array (CA), as illustrated in Figure 2.2. This dipole array's input impedance is formulated to [12]:

$$Z_{in} = \frac{d_x}{d_y} \frac{k_0 \eta_0}{2} \sum_{m_x=-\infty}^{+\infty} \frac{\text{sinc}^2\left(\frac{k_{xm} t}{2}\right)}{(k_0^2 - k_{xm}^2) \sum_{m_y=-\infty}^{+\infty} \frac{J_0\left(k_{ym} \frac{w_s}{2}\right)}{\sqrt{k_0^2 - k_{xm}^2 - k_{ym}^2}}} \quad (2.1)$$

where d_x and d_y represent the dipole spatial periods along the x and y axis, k_0 is the wavenumber in free space, η_0 is the impedance of free space, J_0 is the Bessel function of the zeroth order, k_{xm} and k_{ym} are the x - and y - wavenumber components of the m^{th}

order spatial harmonic or Floquet mode, and t and w_s are the thickness and width of the infinitely long dipoles. By fundamental mode approximation, *i.e.*, $m_{x,y} = 0$, which becomes dominant at lower frequencies, *i.e.*, $k_o \rightarrow 0$, the sinc and Bessel functions can be simplified to an approximate value of 1. Combining this fundamental mode approximation with the scanning angle relations of the x - and y - wavenumber components, the input impedance of the dipole array is represented as [17]:

$$Z_{in} \approx \frac{d_x}{d_y} \frac{\eta_0}{2} \frac{\cos \theta}{1 - \sin^2 \theta \cos^2 \phi} , \quad (2.2)$$

eliminating frequency dependence, and confirming the CSA's relative theoretical infinite bandwidth while approaching a more realizable design.

Further advancement of the CSA into real-world applications as a connected array (CA) of dipoles involves implementation of a ground plane to focus radiation into one of the two bidirectional radiation directions, improving power efficiency and protection of feed network components. However, introduction of a ground plane into the CA antenna significantly changes the input impedance, consequently reducing bandwidth capabilities. When a PEC is placed below a CA of dipoles, the input impedance's reactance becomes strongly inductive, and the radiation resistance approaches zero toward lower frequencies, *i.e.*, since the distance to the ground plane becomes electrically smaller, the array eventually becomes short circuited to the ground plane. Therefore, the reduced bandwidth capabilities become a strong product of these low frequency effects. In order to accurately and efficiently analyze these effects for future design considerations a more thorough model is required.

2.2 Circuit Model Representation

Equivalent circuit modeling of dipole array antennas began with CSA antenna circuit analyses done by Munk [23]. Through these models, Munk was able to develop a solution for ground plane inductance issues. Ideally, the additional strongly inductive reactance added into the antenna circuit would be cancelled out by introducing a negative inductance [24]. Instead Munk refrained from increasing the complexity of the dipole feeding to obtain negative impedance through active elements and proposed a coupling capacitance between the dipole ends. By designing the coupling-ends as interdigital capacitors, the added capacitance could be greatly increased, and precisely controlled to cancel out the ground plane inductance at low frequencies.

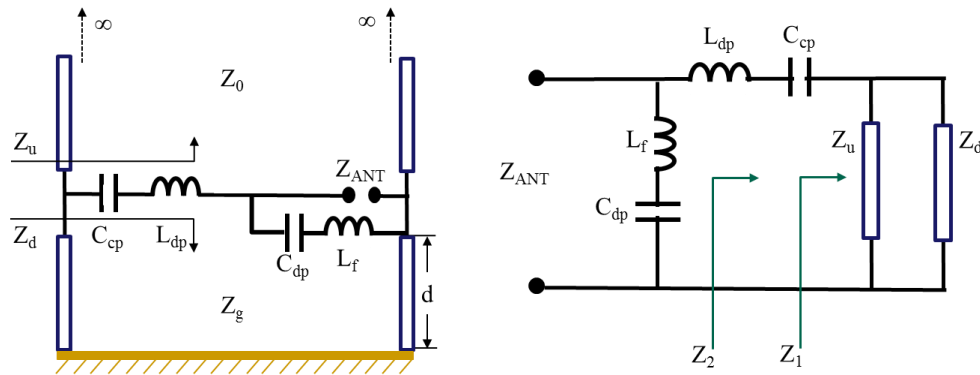


Figure 2.3: Equivalent circuit model for TCA of dipoles positioned above a PEC.

Figure 2.3 illustrates an updated equivalent circuit model for the now infinite tightly coupled array (TCA) of dipoles where C_{cp} is the capacitance between adjacent dipoles and L_{dp} is inductance of the dipoles [25]. In the original equivalent circuit model, Munk didn't account for effects of the dipole feed. Therefore, shunt capacitance, C_{dp} , and inductance, L_f , were introduced to account for dipole feed

coupling. By incorporating these TCA circuit model properties into a CA dipole antenna, as shown in Figure 2.4 (a), with $L_{dp} = 1.68 \text{ nH}$, $C_{dp} = 0.026 \text{ pF}$, $L_f = 0.54 \text{ nH}$, and $C_{cp} = \infty$, the antenna impedance can be derived from the circuit model using Eqs. 2.3-2.7 and compared to HFSS full-wave simulations to verify accuracy.

$$Z_u = Z_0 \quad (2.3)$$

$$Z_d = jZ_g \tan(\beta_g d) \quad (2.4)$$

$$Z_1 = Z_u \parallel Z_d \quad (2.5)$$

$$Z_2 = Z_1 + j\omega L_{dp} + \frac{1}{j\omega C_{cp}} \quad (2.6)$$

$$Z_{ANT} = \left(j\omega L_f + \frac{1}{j\omega C_{dp}} \right) \parallel Z_2 . \quad (2.7)$$

Results from each simulation model are overlaid in Figure 2.4 (b), and confirm the circuit model presented in Figure 2.3 is an accurate tool for modeling CA antennas.

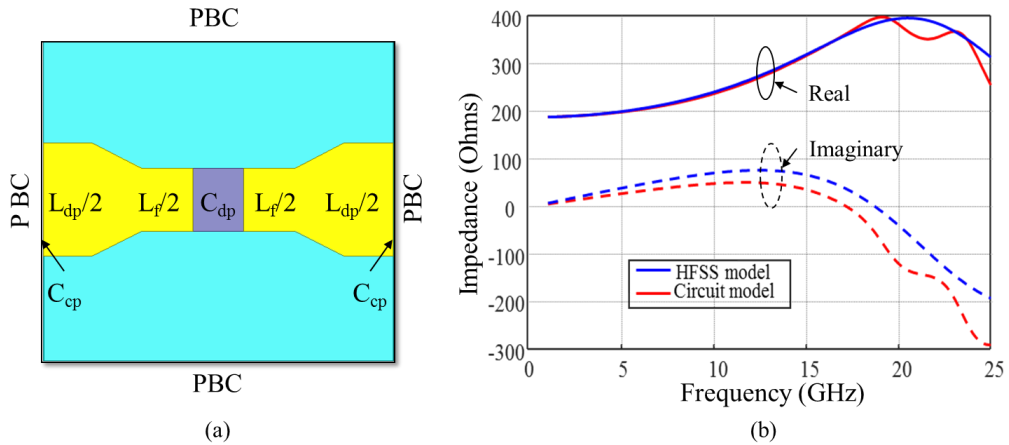


Figure 2.4: (a) Example connected array dipole antenna. (b) HFSS full wave simulation and circuit model comparison of CA dipole antenna.

Use of this circuit model analysis and the dipole coupling capacitance introduced by Munk afforded a near two-fold increase in array bandwidth. Previously, the bandwidth was limited to 2.5:1 by the relation of equation 2.4, *i.e.*, the input impedance of transmission line (TL) traveling through a medium of impedance Z_g shorted at a distance d away from the input. Typically, dipoles in the CA are designed at half the wavelength of the highest operating frequency, $L_{dipole} = \lambda_{min}/2$, to eliminate potential grating lobes. Furthermore, integration of the ground plane into this CA design set a distance, $d = \lambda_{min}/4$, away from the CA plane to achieve maximized broadside radiation, *i.e.*, if $\beta_g = \beta_o = \frac{2\pi}{\lambda}$, then $\beta_g d = \frac{\pi}{2}$, and $Z_d = jZ_g \tan(\beta_g d) = \infty$. With the high frequency bound set, the array bandwidth can be realized by shifting toward lower frequencies until the ground plane distance become electrically smaller, shorting the CA of dipoles. As previously mentioned, this lower frequency limitation set the initial 2.5:1 bandwidth constraint. That is until capacitive cancellation of the inductive reactance allowed for extension of the lower frequency, without effecting the high frequency operation, to provide bandwidths of 4.5:1 [9]. Furthermore, implementation of resistive FSS's and superstrates between the antenna and ground plane, utilizing the $\beta_g = \frac{2\pi n_g}{\lambda}$ relationship to achieve a bandwidth of 21:1 [10].

2.3 Electrical Excitation

Although the advantages seen in demonstrations of the CA and TCA are superior in terms of bandwidth, scan volume, and profile to other UWB antenna array designs, multiple challenges are faced in efforts of efficient excitation of the radiating elements. The primary difficulty with array feeding is a standard 50Ω coaxial cable is not suitable.

2.3.1 Unbalanced Feeding

The dipole elements within CA and TCA antennas are referred to as balanced antennas due to their symmetric geometry. Thus, a balanced feed, *i.e.*, symmetric TLs supplying dipole arms with current of equal magnitude and opposing phase, is necessary to match the balanced nature of the dipoles in order to maintain a uniform current distribution. Traditional power sources driving RF antennas employ 50 Ω coaxial cable RF feeding links based on their 50 Ω output. Unfortunately, coaxial transmission lines are inherently unbalanced resulting in a non-zero net current flow on the outer conductor, producing undesired common mode radiation.

One of the earlier techniques of suppressing these undesirable common mode currents from the coax feed was integrating a “feed organizer” to route 50 Ω coaxial cables to the balanced radiating elements [9, 26]. The feed organizer displayed in Figure 2.5 was fed with two pairs of cables, where outer conductors were grounded to the metal structure while inner conductors were directly connected to the dipole. On the back-end of the cables, 0/180 $^\circ$ hybrid circuits enable a method for supplying the correct phase to each dipole arm [9]. Although this device is able to suppress common mode radiation that degrades array radiation, its physical structure cancels out low-profile properties of CA and TCA antennas. Additionally, mechanical tolerances limit use of feed organizers to lower-frequencies, restricting UWB performance [27].

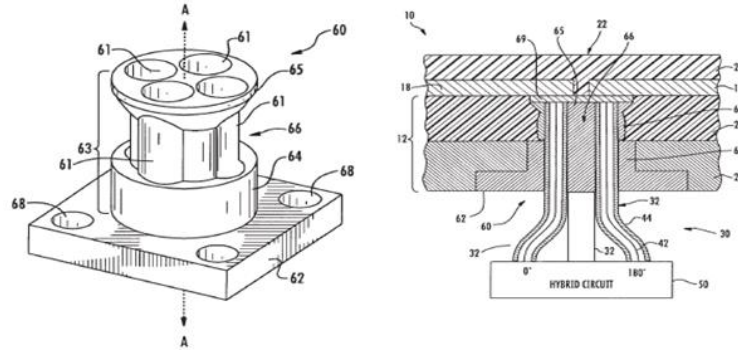


Figure 2.5: Feed organizer used to route coaxial feed to dual-polarization CSA antenna, from [9] [26], © 2009 IEEE.

A different attempt of introducing a balanced feed directly with a coaxial cable without the bulky feed organizer and external hybrid circuit is presented in [28]. In this design, the dipole array is directly connected to a coaxial cable whose outer conductor is soldered to the ground plane, while the inner signal conductor is connected to a coplanar strip (CPS) feeding one of the dipole arms. Coupling the unbalanced coaxial cable to the balanced CPS/dipole produces a radiating TE_{10} -mode resonance (common-mode) via a non-zero net current in the CPS lines, as displayed in Figure 2.6. The solid lines represent the current flow through the CPS and dipoles, and the dotted lines represent the electric field distribution in the mode whose resonant frequency can be formulated as [28]:

$$f_{cm} = \frac{c_o}{2\sqrt{\epsilon_{eff}} \sqrt{D_x^2 + D_y^2}}, \quad (2.8)$$

where D_x and D_y is the spacing between coaxial feed points, and the ϵ_{eff} is the effective dielectric constant between the planes.

Calculation of the fundamental common-mode resonant frequency results in a frequency value located within the desired operational bandwidth. To circumvent this

issue, shorting posts were introduced next to the coaxial cable signal feeds between the dipole and ground plane, enabling a shift of the resonance to higher frequencies by decreasing D_x and D_y [28]. Utilizing this method has afforded a 3:1 bandwidth [27]; however, in conjunction with higher bandwidth array antennas this method becomes a limiting factor of the antenna unit leading to restrictions in application. Additionally, this method does not inherently include any impedance transformation techniques to match the 50Ω coaxial cables. Thus, necessary integration of a dielectric substrate thickened the array by a factor of two, reducing the attractive low-profile nature of the original CSA-based design.

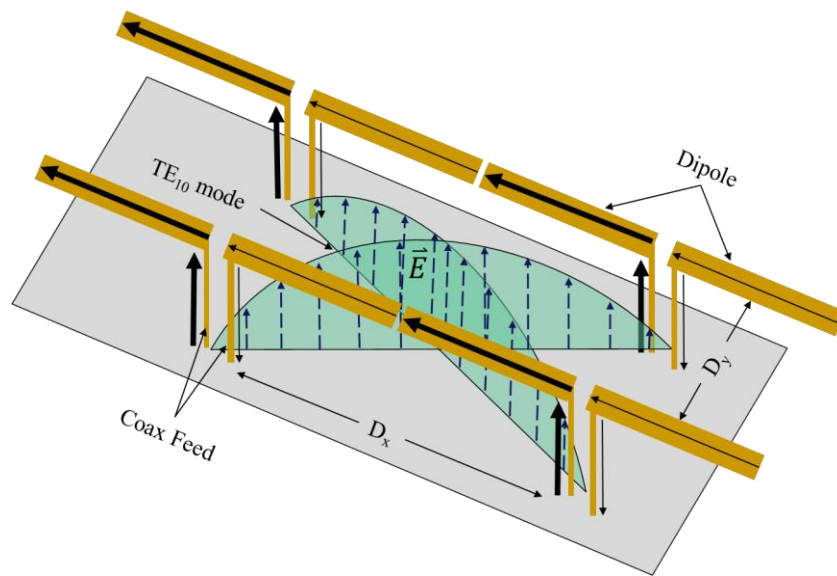


Figure 2.6: Common-, TE_{10} - mode resonance introduced by unbalanced feeding (solid arrows mimic current flow, dotted lines depict electric field associated with common-mode resonance).

2.3.2 Balanced Feeding

Thus far, electrical feeding techniques discussed have primarily focused on introducing components to compensate or control the spurious monopole radiation stemming from a directly integrated unbalanced coaxial cable. One detail neglected by these methods is the approximate 4:1 impedance mismatch between CA/TCA antennas and coaxial cables. In order to satisfy both impedance matching and balanced feed requirements balanced-to-unbalanced transformers, baluns, can be implemented between each coax/antenna element link.

Even though a balun resolves two inceptive difficulties, it is a simplistic solution for a challenging problem and tends to introduce trade-offs between operational frequency, bandwidth, profile, and weight. External baluns have proven capable of performing coplanar waveguide (CPW)/coplanar stripline (CPS), 200Ω to 50Ω transitions; however, this accomplishment comes pairs with high insertion losses up to 3dB and operational frequency restrictions (< 600 MHz) [29]. In contrast, integrated baluns, such as ones based off the coupled ring hybrid design [30-32], provide a planar balanced feed with low insertion loss and high operational frequencies. Precise engineering of the paired feed wires, designed in sync with dipole elements, allows for these advantages, but also introduces limited bandwidth due to the strict dimensional requirements of the ring-hybrid. Lastly, UWB baluns have been developed for high operational frequencies and bandwidth through tapering a microstrip to CPS [33]. Unfortunately, the tapered feed length necessary for operation is proportional to multiple wavelengths of the bandwidth ceiling frequency, making this approach unsuitable when progressive toward operation in the mm-wave regime [42].

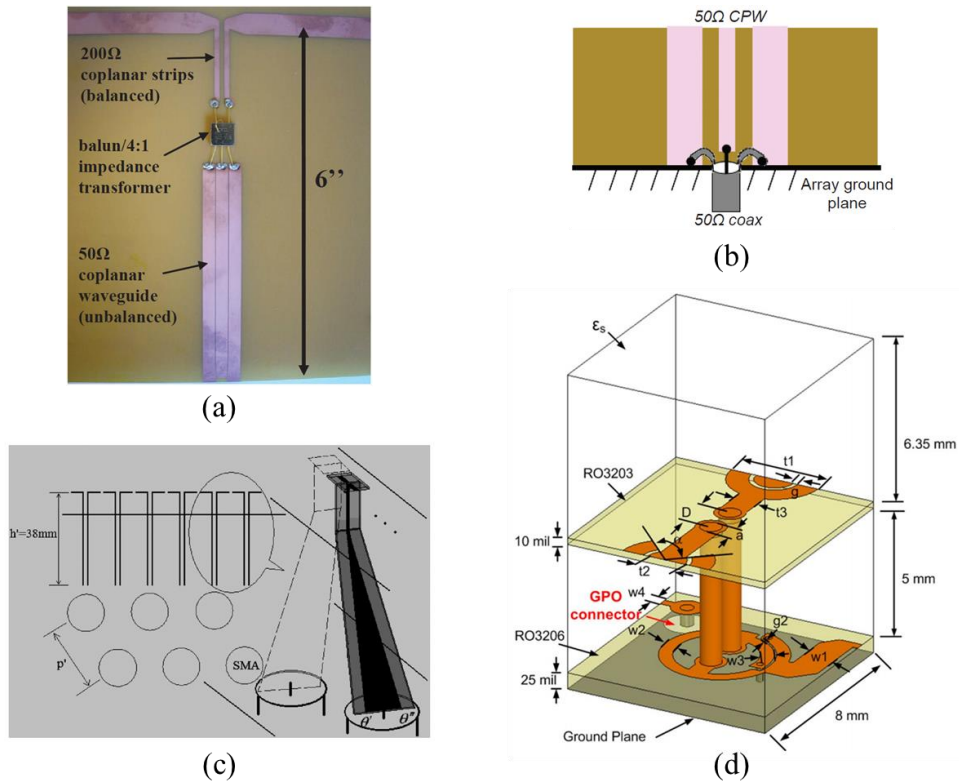


Figure 2.7: (a) External balun linking 50Ω CPW electrical feed and 200Ω CPS of dipole TCA [29], © 2013 IEEE; (b) schematic of 50Ω CPW/coaxial cable connection [29], © 2013 IEEE; (c) UWB balun with microstrip-stripline transition [33], © 2009 IEEE; and (d) Hybrid integrated balun [27] © 2013 IEEE.

Chapter 3

OPTICAL FEEDING PHASED ARRAY ANTENNAS

Optical excitation of antenna arrays serves as an alternative to conventional electrically addressed arrays. By directly integrating a photodiode into each antenna element, one can eliminate the need for any RF feed network. Thus, bulky and expensive RF cables can be replaced with optical fibers, which are inherently light, low-loss, and immune to electromagnetic interference. Furthermore, maintaining a balanced signal towards each antenna is straightforward using a photodiode integrated proximal to each dipole element. This eliminates common-mode resonance, which typically disrupts electrically fed array operation, thereby making bandwidth-limiting baluns unnecessary [44].

Tightly spaced photodiodes provide a nearly ideal current source, allowing close approximation to Wheeler's theoretical current sheet that would otherwise not be possible using conventional electrical feeding at high frequencies and operational bandwidths. However, the introduction of an optical feed network does not eliminate the difficulties in designing wideband antenna arrays, it only shifts them from the RF circuitry to the photodiode. Robust and efficient alignment of high-power optical inputs to high frequency, micron-scale photodiodes can be challenging without introducing some loss into the system. Notably, introducing a ground plane behind the array while maintaining a fiber-feed to the photodiodes is a concern. Each photodiode also requires a carefully applied bias across their junctions for efficient high-frequency operation. If the bias lines are not designed appropriately they can introduce

resonances of their own into the RF system, limiting array bandwidth analogous to the common-mode resonances seen with electrical feeding [44].

Fortunately, while these problems are non-trivial, solutions have been proposed in the literature [34-36], and appropriate design and fabrication techniques, presented in Chapter 4 and 5, can effectively deal with these issues. Historically the biggest deterrent in the adoption of optically fed arrays has been the low power output per antenna element, *i.e.*, the power handling of the photodiodes. While commercial photodiodes can achieve bandwidths between 50 and 100 GHz, frequencies regimes that would make for impressive arrays, their output powers are typically limited to less than 10 dBm. For optically fed arrays to become routinely integrated into functioning systems, high-power photodiodes must be developed to solve this fundamental power output problem [44].

3.1 Modified Uni-Traveling Carrier Photodiodes

Recently, state of the art MUTC photodiodes, designed at the University of Virginia and currently fabricated at University of Delaware, Figure 3.1, have been able to output over 1 W of power at 10 GHz under continuous wave operation [37]. The epitaxial structure of the diode is designed so that the electric field within the junction is predistorted in order to maintain a smooth bias field during high current operation. Due to this epitaxial design, RF output power is primarily limited by thermal burnout of the device, *i.e.*, the photodiode overheats at high optical input powers, rather than space-charge effects. Therefore, time-multiplexing the optical input to the photodiode using pulsed power modulation can be used to improve power handling even further, and peak powers of over 10 W have been reported at 10 GHz using low duty cycles, which may be useful for longer range wireless links [38] [44].

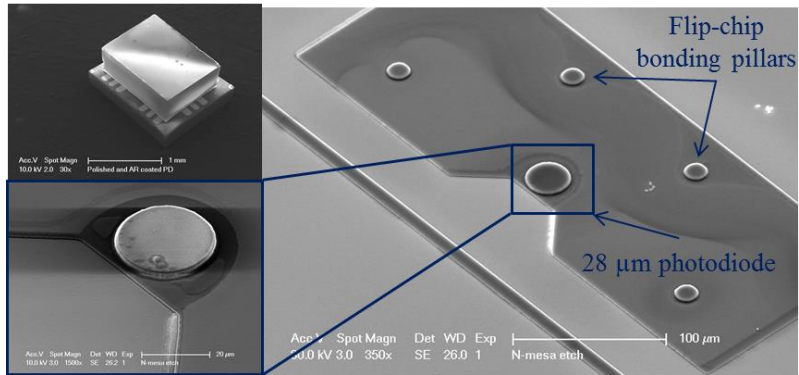


Figure 3.1: 28 μm diameter MUTC photodiode fabricated at University of Delaware.

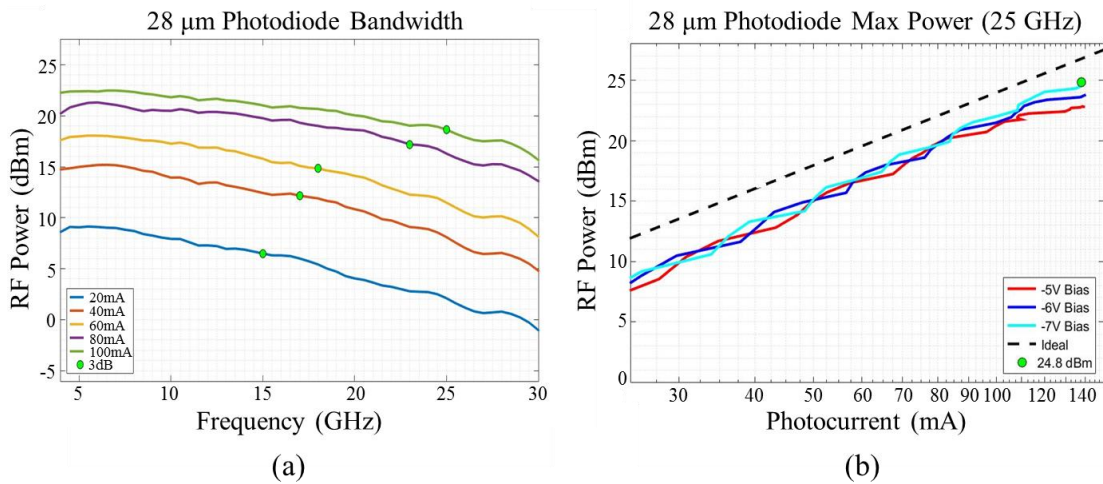


Figure 3.2: (a) Bandwidth performance of 28 μm diameter photodiode, and (b) power output of approximately 24.8 dBm at 25 GHz.

In order to leverage the exceptional power handling of the MUTC photodiodes for array excitation, the system must be designed with thermal management in mind. Sub-mounts made of high thermal conductivity aluminum nitride (AlN) or diamond are required in order to disperse the thermal output of each photodiode. Then the high-

power photodiodes must be flip-chip bonded to this substrate using gold-gold thermo-compression bonding in order to maintain an effective thermal pathway into the antenna substrate. Figure 3.2 above shows the power handling and bandwidth capabilities of a 28 μm MUTC photodiode flip-chip bonded to an AlN sub-mount, which was fabricated at UD in collaboration with UVA [44].

3.2 Ultra-Wideband Feed Network for Photonic Phased Arrays

3.2.1 UWB Tunable Photonic RF Signal Generation

While MUTC photodiodes can provide optically fed arrays with the RF power output they need to be competitive with conventional electrically fed systems, the diodes need to be excited using a low-noise RF source in order to demonstrate efficient beam steering. Simple heterodyning of 2 lasers onto the photodiodes would result in excess system noise and spurious beam generation that would limit system performance at high-output powers. Therefore, an injection-seeding based source to correlate phase noise between the feed lasers and greatly suppress spurious noise developed at the University of Delaware has been selected for microwave photonic signal generation. This source is capable of providing signals from 0.5 to 110 GHz with a linewidth <1 Hz and ultra-low phase noise [21] [44].

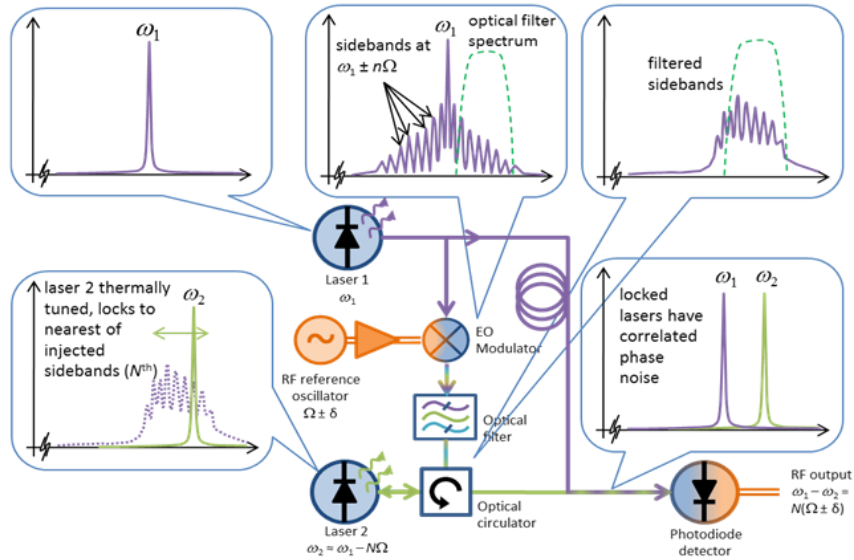


Figure 3.3: Schematic of photonic radiofrequency signal generation system [21]. Image courtesy of Dr. Garrett J. Schneider.

As illustrated in Figure 3.3, the signal generation system utilizes two semiconductor lasers capable of being thermally tuned over THz ranges for necessary wide tuning abilities in heterodyne detection on the photodiodes. However, for high-purity signal generation, the heterodyne process needs to incorporate two coherent optical signals. This can be accomplished by modulating a local oscillator (LO) reference signal onto a master laser, filtering out the carrier and lower modulation-sideband comb, and injecting the upper modulation-sideband comb into the slave laser for phase locking. If equal channel path length is assumed, it is possible for cancellation of optical phase noise produced through the spontaneous emission process. By using this technique, precise tuning of the reference oscillator and rough thermal tuning of the slave laser affords selection of modulation-sideband harmonics,

which results in widely tunable, spectrally pure, low-noise RF carriers that form the basis for the phase control network discussed in the next section.

3.2.2 Phase Control Network

This low-noise system can be used in conjunction with a dual-polarization, optical interleaving feed network to provide the MUTC photodiodes with a clean RF signal [20]. The network exploits polarization maintaining fiber and polarization dependent phase modulators to mitigate the effects of acoustic vibration on the incident fiber-optic signals. Additionally, the photocurrent from the MUTC diodes can be monitored to provide feedback to the feed network's polarization controllers in order to suppress phase drift. This novel feed architecture [20] combined with the practically unlimited bandwidth of optical fiber can be used to simultaneously drive multiple high-fidelity beams over a wide operational bandwidth [44].

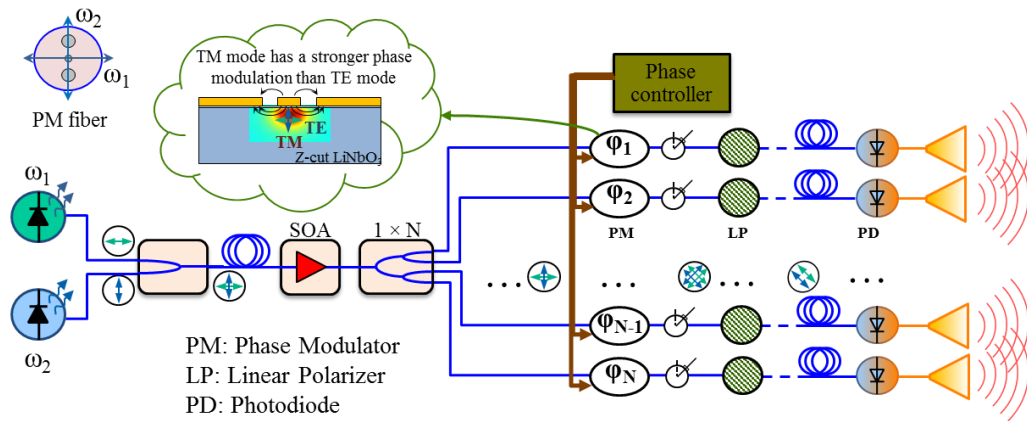


Figure 3.4: UWB phase control optical feed network [20]. Image courtesy of Dr. Shouyuan Shi.

The optical phase feed network, displayed in Figure 3.4, begins with two coherent optically paired sources of frequency ω_1 and ω_2 launched orthogonally on the fast and slow axes of a single polarization maintaining (PM) fiber, yielding the following optical signal:

$$E_0 = \hat{x}E_x e^{j(\omega_1 t + \varphi_1(t))} + \hat{y}E_y e^{j(\omega_2 t + \varphi_2(t))}, \quad (3.1)$$

where E_x and E_y are the electric field magnitudes located in the slow and fast axes of the PM fiber, and $\varphi_1(t)$ and $\varphi_2(t)$ represent corresponding phase fluctuations. This combined optical signal is then amplified, and split into N channel before being fed into an EO phase modulator. Coupling of the PM fiber and EO phase modulator is accomplished by aligning fast and slow axes to TE and TM modes experienced in LiNbO₃ [18]. A representation of the axes/mode alignment can be seen in Figure 3.4

Each modulator will subsequently be fed a modulation bias voltage, V_m , to induce EO modulation on each polarized axes. For z -cut LiNbO₃, TE and TM modulation is unequal due to EO coefficient offsets between the r_{33} and r_{13} tensors causing a phase difference between the two optical modes. This effect can be realized as:

$$E_{PM} = \hat{x}E_x e^{j\left(\omega_1 t + \varphi_1(t) + \frac{\pi V_m}{V_\pi}\right)} + \hat{y}E_y e^{j\left(\omega_2 t + \varphi_2(t) + \frac{\pi V_m}{3V_\pi}\right)}, \quad (3.2)$$

where V_π is the voltage necessary to induce a π phase shift on the optical signal, *i.e.*, the half-wave voltage. This difference, *i.e.*, modulation efficiency between the 2 polarizations allows for a tunable phase shift of the heterodyning signal.

Next, the combined phase modulated signals transmit through a 45° rotational key for projection of each signal onto both the fast and slow axis of the PM fiber before filtering out one overlapped pair by a linear polarizer. This deliberate rotation

of both optical signals eliminates orthogonality cancellation while the linear polarization filter sets both signals for interference on the photodiode fed by a single-mode fiber. A representation of the rotated, linear polarization filtered field can be expressed as the following:

$$E_3 = \frac{\sqrt{2}}{2} \left(E_x e^{j\left(\omega_1 t + \varphi_1(t) + \frac{\pi V_m}{V_\pi}\right)} + E_y e^{j\left(\omega_2 t + \varphi_2(t) + \frac{\pi V_m}{3V_\pi}\right)} \right). \quad (3.3)$$

A $\sqrt{2}/2$ factor is added into the expression to account for 3-dB polarizer loss. Lastly, the signal is photomixed onto the photodiodes to generate an RF photocurrent:

$$I_{RF} = \frac{1}{2} \Re E_x^2 E_y^2 \cos \left((\omega_1 - \omega_2)t + \varphi_1(t) - \varphi_2(t) + \frac{2\pi V_m}{3V_\pi} + \frac{\omega_1 - \omega_2}{c} n_o L \right), \quad (3.4)$$

where \Re represents the responsivity of the photodiode, $\omega_1 - \omega_2$ is the RF current angular frequency, c is the speed of light, and n_o and L are index and length of single-mode fiber, respectively.

A clear advantage of this system is the phase change effect occurring in a single fiber so that noise is minimized. Since both signals detected at each photodiode are combined then split into channels of equal length, phase noise experienced by each signal will cancel out at the photodiodes, *i.e.*, $\varphi_1(t) = \varphi_2(t)$. Also, additional noise contributed by the single-mode fiber, $[(\omega_1 - \omega_2)/c] n_o L$, can be significantly reduced, by again, keeping the L of each channel equivalent, as well as bundling fibers together to experience similar acoustic and thermal variation [20]. The last remaining phase term relates to the phase modulators used to control the beam steering. By biasing the modulators, a progressive phase is projected across array antenna elements to shift beam directionality at angle, θ . Beam steering can be control the relation:

$$\Delta\varphi = k_{RF} d \sin \theta = \frac{2\pi V_m}{3V_\pi}, \quad (3.3)$$

where d is the array antenna element separation and k_{RF} is the wave vector of the RF signal.

3.3 Conclusion

By pairing the University of Delaware's RF source capable of providing low-noise, high purity signals from 0.5 to 110 GHz with the phase control network, UWB steering capabilities are enabled. Addition of MUTC photodiodes, extends system performance to encompass high power and linearity while maintaining bandwidth applicable to desired communication systems. In order to fully maximize the Tx system, a CA antenna should be designed to balance performance previously demonstrated by CSA based arrays while incorporating coupling of optical phase feeding components.

Chapter 4

PHOTODIODE-COUPLED ANTENNA DESIGN AND MODELING

4.1 Photodiode-Coupled Antenna Model

Utilizing CSA concepts and MUTC photodiodes, a photodiode-coupled CA antenna designed for UWB operation is presented. Circuit and HFSS full-wave modeling techniques were used to characterize and tune design parameters. For a complete analysis of the hybrid RF-phonic antenna, both the photodiode and antenna can be separately modeled before investigating the coupling of each device into one Tx sub-system.

4.1.1 Connected Array Model

Replication of Wheeler's CSA impedance characteristics began by designing a hybrid bow tie/dipole antenna unit cell and duplicating it along the x - and y - axis to construct a CA. Each unit cell radiator carries a dynamic load factor associated with the excitation sources which determines the overall CA performance, making large arrays computationally intensive. In order to simplify and accelerate computation of the array properties, uniformity in excitation sources for both amplitude and phase is applied through a unit cell expansion into a 2D infinite array. Implementation of this infinite array model provides an accurate approximation for larger arrays, *i.e.*, 10 x 10 and greater.

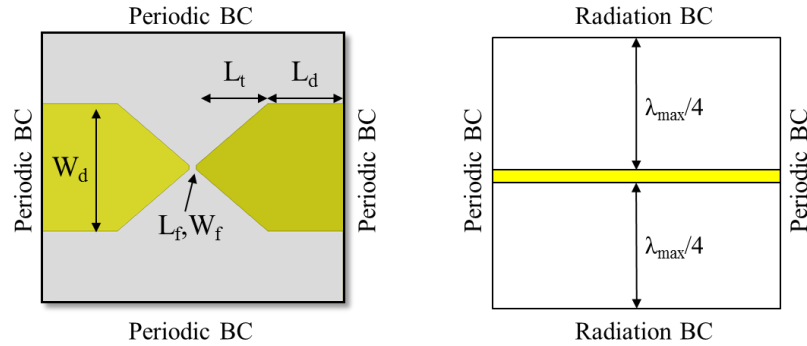


Figure 4.1: Simulation model of infinite hybrid bow tie/dipole antenna where $L_f = 0.15$ mm, $L_t = 1.5$ mm, $L_d = 1.6$ mm, $W_f = 0.1$ mm, and $W_d = 3.0$ mm.

A top- (left) and side-profile (right) view of the hybrid bow-tie/dipole antenna unit cell can be seen in Figure 4.1. Period boundary conditions (BC) surround the outer edges for planar replication of the unit cell, and are capable of simulating beam steering operation through phasing adjacent walls (left-right wall pair and top-bottom wall pair). Radiation BC (absorption BC) are set $\lambda/4$ at the longest desired operating wavelength away for emulation of free-space radiation in the \pm broadside directions. In this case phase delay between PBC walls is set to zero, inducing maximized broadside radiation due to no scanning. Analysis of the design is performed using High Frequency Structure Simulator (HFSS), a commercial full-wave electromagnetic modeling software developed by ANSYS.

Lumped port sources applied at the inner feed point of the dipole arms were used as the antenna excitation method. The impedance of the lump port was varied from 50 - 1000 Ω and the frequency was swept from 0.5 – 20GHz at each port impedance. Figure 4.2 shows the simulated active impedance results of the infinite CA antenna. Results for the active resistance and reactance both converge to the

theoretically predicted values at low frequencies, 188Ω and 0Ω respectively. When sweeping towards higher frequencies resistance increases to roughly 210Ω and the antenna becomes slightly capacitive. Additionally, active impedance properties remained independent of all lumped port impedances to verify expectations of non-source impedance susceptibility. Overall, based on these results the design satisfies all anticipated properties of the CSA model.

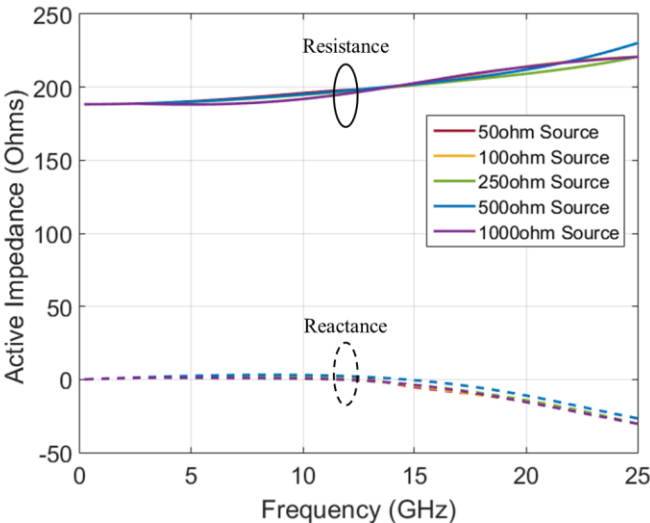


Figure 4.2: Simulated active resistance and reactance results of infinite CA.

4.1.2 Coupling Photodiode to CA Antenna

A photodiode-coupled CA antenna can be realized through the conceptual CSA design illustrated in Figure 2.2, where the current sources exciting the dipole elements are photodiodes. Each photodiode is modeled as a parallel ideal current source, capacitor circuit. The CA antenna is represented by a parallel resistor/capacitor circuit derived from the antenna characteristics extracted from simulation results discussed in the previous section. Connecting each of these equivalent circuits in

parallel affords a representation of the photodiode-coupled CA antenna, as shown in Figure 4.3. Analysis of this equivalent circuit model provides the necessary terms to evaluate the performance of the photodiode-coupled antenna, namely radiated power, bandwidth, and power efficiency.

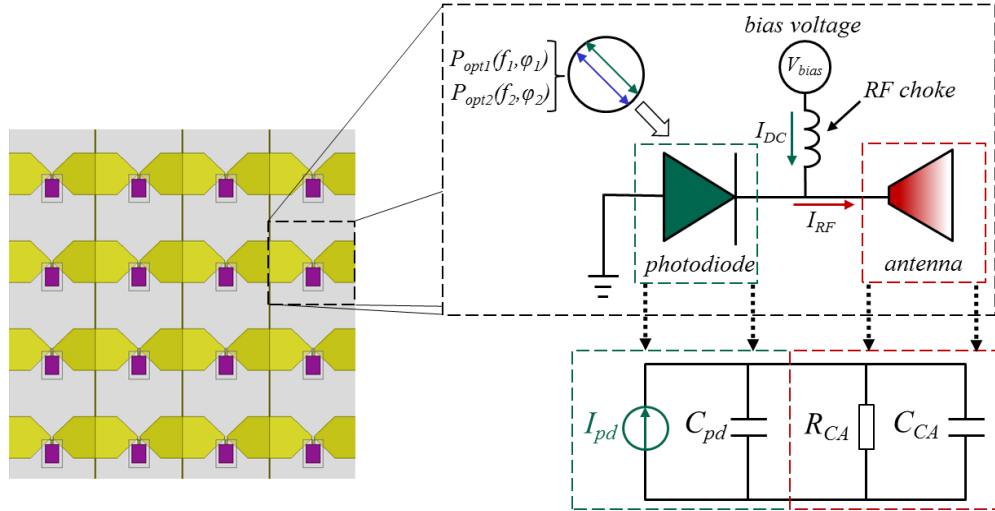


Figure 4.3: Equivalent circuit representation of photodiode-coupled CA antenna.

Further illustration in Figure 4.3 shows the photodiode provided concurrently with reverse biased through an inductor, *i.e.*, rf choke, and an incident two-tone optical signal to generate photocurrent given by [21]:

$$I_{pd}(f_{RF}) = \Re \sqrt{2P_{opt1}P_{opt2}} H(f_{RF}) e^{j(2\pi f_{RF}t + \phi_{RF})}, \quad (4.1)$$

where $f_{RF} = f_{opt1} - f_{opt2}$ is the frequency and $\phi_{RF} = \phi_{opt1} - \phi_{opt2}$ is the phase of the RF photocurrent, while \Re and $H(f_{RF})$ represents the photodiode responsivity and frequency response, respectively. This current will subsequently drive the CA antenna element to radiate RF power, represented as:

$$P_r(f_{RF}) = \frac{\frac{1}{2} I_{pd}^2 R_{CA}}{1 + (2\pi f_{RF} R_{CA} (C_{pd} + C_{CA}))^2}. \quad (4.2)$$

Both circuit terms, R_{CA} and C_{CA} , for the CA antenna can be extracted from the infinite array simulation results. Furthermore, the frequency response, $H(f_{RF})$, enables the photodiode capacitance to be estimated as:

$$C_{pd} = \frac{1}{100\pi B_{pd}}, \quad (4.3)$$

where the term B_{pd} represents the 3-dB bandwidth of the photodiode loaded with a load of 50Ω , $R_L = 50\Omega$,

$$B_{pd} = \frac{1}{2\pi R_L C_{pd}}. \quad (4.4)$$

Maximum radiated power can be realized by shifting operational frequency toward DC,

$$P_{r\max}(f_{RF}) = \frac{1}{2} I_{pd}^2 R_{CA}. \quad (4.5)$$

Next, by sweeping away from DC to higher frequencies, the operational frequency range is determined by the cutoff frequency, f_c , marking 3-dB roll off of radiated power. This operational bandwidth is conveyed as:

$$BW = f_c = \frac{1}{2\pi R_{CA}(C_{pd} + C_{CA})}. \quad (4.6)$$

From these expressions, it is apparent that there is a trade-off between radiated power and bandwidth in relation to impedance. In a practical sense, this trade-off will be balanced by selecting the largest photodiode capable of satisfying antenna bandwidth requirements for maximized radiated power within that band. Furthermore, the bandwidth and radiation power per photocurrent squared can conveniently be used as a figure of merit for both photodiode-coupled CA antenna performance and transmission information capacity [36],

$$\frac{BW \cdot P_{r\max}}{I_{pd}^2} = \frac{1}{2\pi(C_{pd} + C_{CA})}. \quad (4.7)$$

Another figure of merit for the antenna is the ratio of radiated power, P_r , to total power consumption, referred to as power efficiency,

$$\eta = \frac{P_r}{P_{opt1} + P_{opt2} + P_{dc}}. \quad (4.8)$$

The total power consumed by the photodiode-coupled CA antenna consists of total incident optical power, $P_{opt1} + P_{opt2}$, and DC power product of the reverse bias voltage and DC photodiode current, P_{dc} . In order to maximize radiated power and linearity, each two-tone signal optical power component should have equal power, *i.e.*, $P_{opt} =$

$P_{opt1} = P_{opt2}$, and the photodiode should be supplied with a minimum bias voltage, $V_{minbias} \approx \sqrt{2}I_{ph}R_{CA}$, to minimize the DC power consumption to:

$$P_{DC} \approx \sqrt{2}\Re P_{opt} I_{pd} R_{CA}. \quad (4.9)$$

Using these conditions, the maximum power efficiency is equated to:

$$P_r(f_{RF}) = \frac{\Re^2 H^2(f_{RF}) I_{opt} R_{CA}}{1 + 2\Re^2 H^2(f_{RF}) I_{opt} R_{CA}}, \quad (4.10)$$

resulting in a theoretical power efficiency limit of 0.5.

4.2 Infinite Photodiode-Coupled Array Antenna Modeling

Creation of a theory-matched CA antenna and reliable photodiode model sets a foundational starting point for designing a photodiode-coupled CA antenna complete with all necessary optical excitation components. Formulation of the 3D antenna model and associated operating principles including antenna structure, optical integration components, BCs, and beam steering parameters was completed in MATLAB (Mathworks). Design parameters, beginning with the CA dimensions in Figure 4.1, were input and swept for substrates, photodiode biasing circuitry, optical excitation components, and photodiode electrical connection placement. Execution of the MATLAB parametric analysis control script generates a visual basic script to interface with the High Frequency Structure Simulator (HFSS) 3D full-wave electromagnetic field solver (ANSYS) to solve for the antenna's active S-parameters. These real and imaginary S-parameters are exported, and imported back into MATLAB where they merge with the photodiode model to calculate active input impedance, far-field and gain profiles, and radiated power.

4.2.1 HFSS Full-Wave Electromagnetic Modeling Studies

Four main design characteristics were taken into consideration: substrate material and thickness, bias circuitry dimensions and position, optical excitation method/components, and photodiode electrical feeding of the dipoles. Each design factor was implemented in sequential series, as listed, to study the effects on active input impedance, far-field and gain profiles, and radiated power. All components added into the model must be characterized in this manner due to the introduction of parasitic reactance. A few parasitic reactance examples are: 1) adding the photodiode will likely introduce a height offset from the dipole leading to parasitic capacitance, 2) electrical connection of the photodiode through either wire bonds or flip-chip bonding produces inductance, and 3) optical alignment components, *i.e.*, GRIN lens, optical fiber ferrules, and ferrule mounts, of various dielectric properties present parasitic reactance too. Optimization of each design characteristic was complete before addition of the next variable. Focus of results was placed on reduction of the photodiode capacitance and CA resistance and capacitance, $R_{CA} (C_{pd} + C_{CA})$, while limiting parasitic reactance until the desired operational bandwidth of 5-20 GHz (4:1) was achieved over a significant steering range.

4.2.1.1 Substrate

As previously mentioned, the photodiode epitaxial structure is designed so that the RF output power is primarily limited by thermal burnout. Ideally, the antenna substrate would operate on a TEC ground plane; however, as compensation balance between high photodiode output power and high antenna radiated power, a largely thermally conductive material is used as the antenna substrate. Additionally, the substrate should have a relatively low permittivity to reduce defects in radiation. AlN

was selected in remaining consistent with sub-mounts routinely used as a heat sink for completed MUTC photodiodes. Although AlN's dielectric constant is not significantly large, $\epsilon_{r,AlN} = 9$, any permittivity-related radiation effects from the material are able to be minimized by controlling substrate thickness.

Simulation of AlN effects on active impedance and radiated power were accomplished by adding a substrate to the infinite array model presented in Section 4.1.1 and sweeping thickness from 0 μm to 500 μm . The relation of substrate thickness and impedance can be realized by adding an AlN slab between the antenna and infinite free space in the CA dipole antenna circuit model, Figure 2.3, then adjusting the transmission line impedance equation to yield:

$$Z = Z_{AlN} \frac{Z_0 + jZ_{AlN} \tan(\beta_1 d_{AlN})}{Z_{AlN} + jZ_0 \tan(\beta_1 d_{AlN})}, \quad (4.11)$$

where Z_{AlN} is the impedance of AlN ($Z_{AlN} = Z_0/\epsilon_{r,AlN}$), Z_0 is the impedance of free space, β_1 is the wavenumber in the AlN slab, and d_{AlN} is the thickness of AlN.

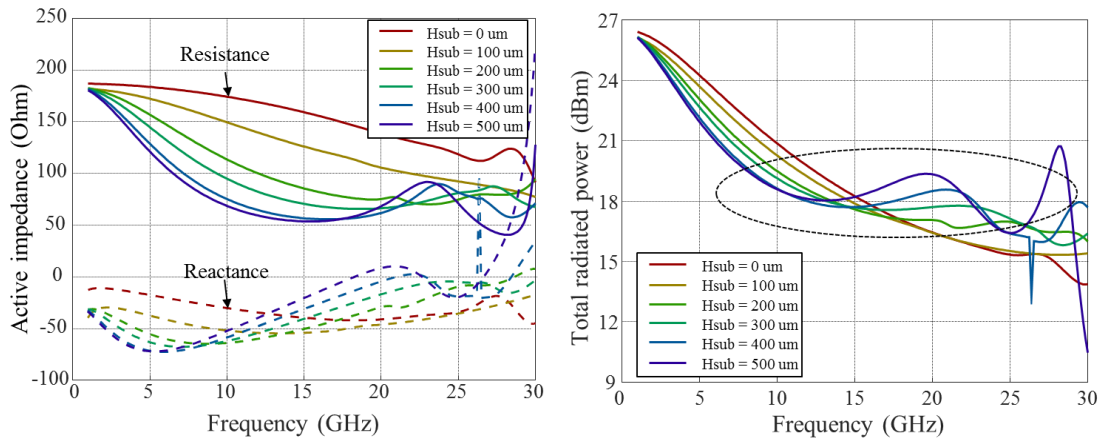


Figure 4.4: Simulated aluminum nitride substrate effect on active radiation impedance and total radiate power at 70 mA photocurrent.

As shown in Figure 4.4, and verified in equation 4.11, increasing substrate thickness reduces the radiation resistance significantly at frequencies greater than 5 GHz while the reactance increases, becoming more inductive. Initially it appears as if thicker substrates are the best option due to the lower radiation impedances necessary for large operational bandwidth; however, potential introduction of substrate modes risk degradation of beam steering range and radiation efficiency [39]. Contrarily, AlN is brittle and is difficult to produce at extremely thin substrates ($< 200 \mu\text{m}$), and its thermal sinking abilities also decrease. Thus, a substrate thickness of $250 \mu\text{m}$ was selected to balance these negative effects while affording relatively flat radiated power over a wide frequency band.

4.2.1.2 Bias Line Circuitry

Effective photodiode operation requires a DC biasing network to supply a reverse bias to each active photodiode-coupled CA antenna element. Ideally, the biasing circuitry should remain simple and introduce negligible effects to antenna radiation. To accomplish these goals, bias lines were designed perpendicular to the dipole arm length direction creating cascaded biasing of multiple adjacent antenna elements at once, as shown in Figure 4.5. Additionally, bias line position and width were carefully selected to ensure only DC current flow and minimal scan blindness from resonances.

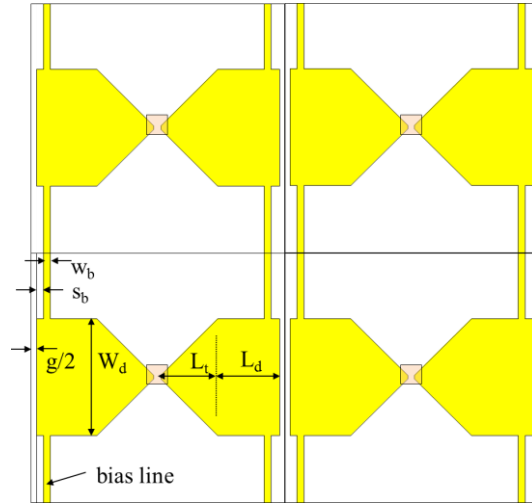


Figure 4.5: Bias line network for photodiode-coupled CA antenna, $g/2$ is the capacitive coupling gap between dipole edges, s_b is the spacing of the bias line from the edge of the dipole, and w_b is the bias line width.

To guarantee the bias lines are fed with only DC current, each bias line should be positioned away from strong RF current distribution. Thus, DC bias lines were set flush with the outer edge of the dipoles, $s_b = 0$, due to RF current being applied at the inner feed points. Additionally, sweeping the bias line position verified that at $s_b = 0$ shifts resonance induced by bias lines to a higher frequency, *i.e.*, decreases the capacitance created between bias lines leading to an increased resonance frequency. These effects are illustrated in Figure 4.6. By implementing outer edge positioning of the DC feed, direct connection of the dipoles is not achievable due to opposing bias on connected arms. Therefore, a small gap of $5 \mu\text{m}$ was introduced to act as a DC current block while still appearing connected at microwave frequencies.

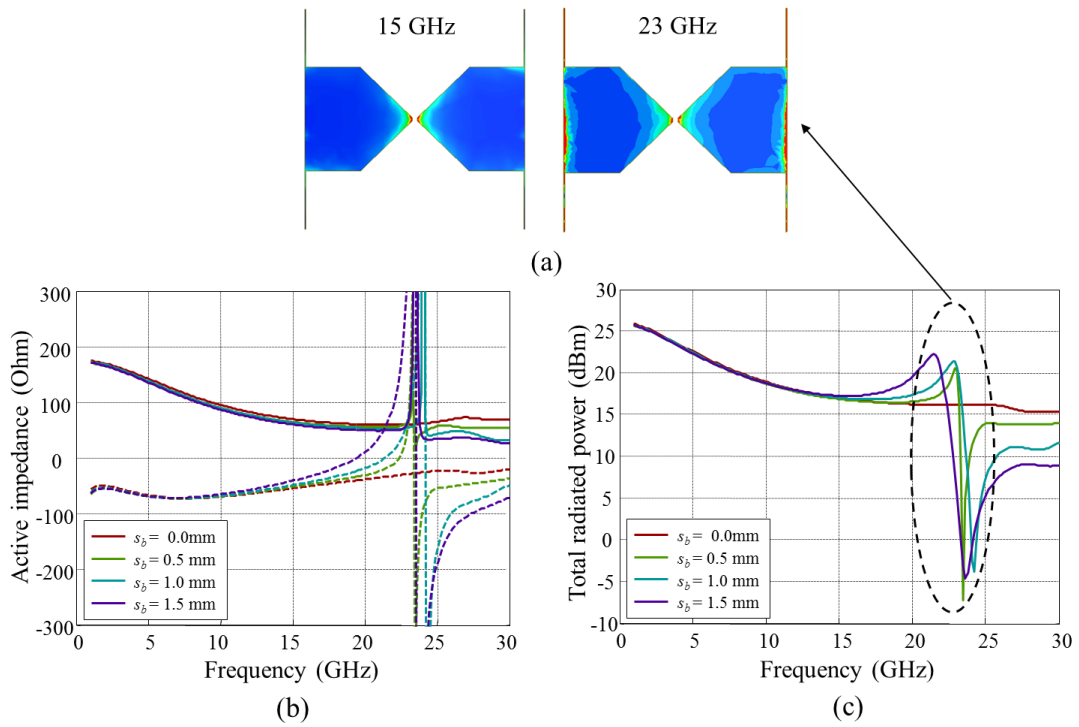


Figure 4.6: (a) Surface current distributions at working 15 GHz and resonant 23 GHz, (b) active impedance response to s_b sweep, solid lines represent resistance and dotted represent reactance, and (c) total radiate power.

Although positioning of the bias line aids in reducing resonances detrimental to radiation and beam steering, dimensional parameters, namely length and width, still pose risks associated with antenna impedance and scan blindness. For length, the bias lines in each dipole unit cell need to be designed less than half a wavelength at highest operating frequency. Taking into account the antenna substrate yields the following bias line design length relation,

$$L_b \leq \frac{\frac{1}{2}\lambda_{\min}}{\sqrt{\frac{1}{2}(\varepsilon_r + 1)}} , \quad (4.12)$$

in which L_b , λ_{\min} , and ε_r are the bias line length, wavelength at highest operating frequency, and dielectric constant of the substrate, respectively. Selecting a width requires balancing a size trade-off; too large of a bias line width will introduce and shift a resonance towards lower frequencies in a similar way with shifting the line away from the dipole edge, too small of a width will drastically increase electrode resistance in the line. Final length and width dimensions satisfying all requirements are $L_b = 6.355$ mm and $w_b = 30$ μm , both of which are incorporated into the results shown in Figure 4.6.

4.2.1.3 Optical Alignment Components

Completion of the minimal electrical component design allows for expansion into optical components necessary for implementation of the optical phase feed network. Since the photodiode will be fed a two-tone optical signal through a single-mode fiber, a small optical alignment system needs to be designed to focus the optical power from the single-mode fiber to the 28 μm photodiode gold-gold thermo-compression flip-chip bonded to the dipoles. Uniform illumination of the photodiode junction requires a lens for controlled focusing of light; therefore, the alignment system will consist of an optical fiber ferrule for robust alignment with a graded-index (GRIN) lens to focus the light, and a mount to secure the focusing components to the antenna. An example of this set-up is illustrated in Figure 4.7.

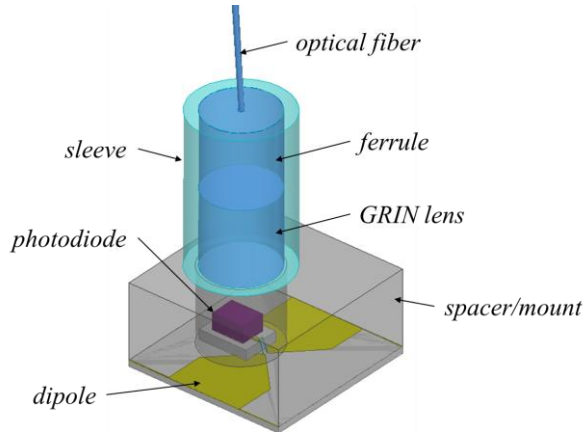


Figure 4.7: Initial proposed optical feed integration technique for CA antenna.

Dimensions and positioning of the GRIN lens and single-mode pig-tailed fiber ferrule were based off of components purchased from Thorlabs, Inc. Both the GRIN lens and fiber ferrule are made from oxide glass with a diameter of 1.8 mm and length of 5.6 mm. The mating sleeve has an inner diameter of 1.818 mm, outer diameter of 2.8 mm, length of 10 mm, and is made out of borosilicate glass. Additionally, a fiber spacer/mount was designed to position the GRIN lens output approximately 2 mm away from the photodiode, matching its effective focal length.

Since the GRIN lens, mating sleeve, and pig-tailed fiber ferrule are all components purchased from Thorlabs, Inc. their physical properties are fixed; therefore, direct input of the dimensions and material properties is all that can be done for modeling. On the other hand, the fiber mount allows for flexible design in order to optimize antenna performance. A good spacer/mount should provide exceptional stability to maintain light-to-photodiode coupling in addition to being low-dielectric for minimizing back-radiation towards the feed network, as well as low loss [40]. Based on this criteria, it was determined that these spacer/mounts could be 3D printed,

with low fill-factor ABS material, for increased structural design flexibility and the capability of minimizing dielectric-induced radiation effects. First, the spacer/mount was designed structurally to support the optical alignment components since material properties are more flexible to implement. Once a reliable structure for holding the sleeve was finalized, different forms of the spacer body were simulated to determine the best way to minimize dielectric effects, shown in Figure 4.8. As expected, and displayed in Figure 4.9, the results from the four test cases verified that as a spacer/mount approaches an effective dielectric constant of free space, impedance and radiated power results are optimized.

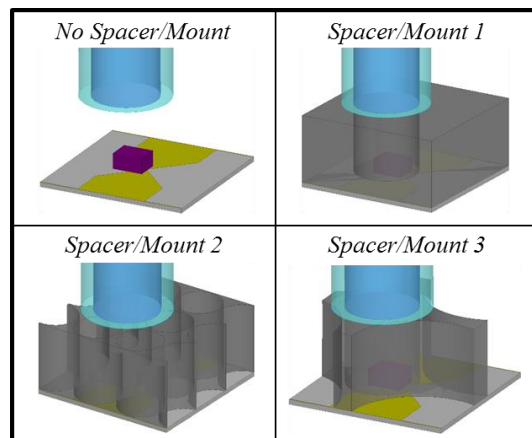


Figure 4.8: Spacer/mount body designs made out of ABS, a common 3D printed material, to reduce dielectric effects.

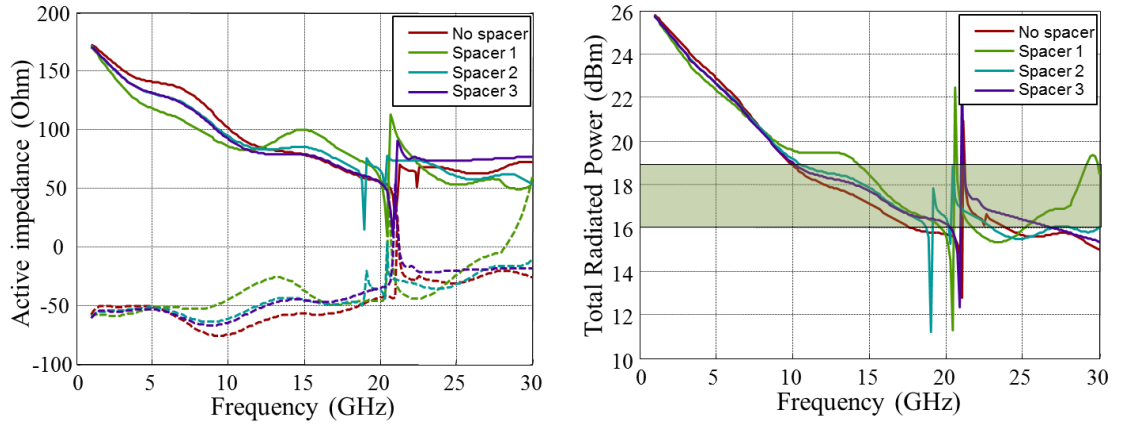


Figure 4.9: Simulated spacer/mount effects on active radiation impedance and total radiate power at 70 mA photocurrent.

The resonance effects seen with the fuller spacer/mounts are introduced through the interaction between the bias line circuitry and the spacer material. Essentially, the added spacer sandwiches the bias line between ABS and AlN media, increasing the effective bias line length to,

$$L_{eff} \approx \sqrt{\frac{\epsilon_{r,AlN} + \epsilon_{reff,ABS}}{2}} L_b \quad (4.13)$$

where $\epsilon_{r,AlN}$ is the permittivity of AlN, $\epsilon_{reff,ABS}$ is the effective permittivity of ABS, and L_b is the physical bias line length. As the effective length increases, it begins to violate the relation in equation 4.12, therefore introducing a resonance at lower frequencies. Overall, spacer/mount design #3 provides the best results out of the design approaches.

4.2.1.4 Inductive Peaking

Incorporating all the fundamental operation components for an optically-excited CA antenna has resulted in a 2:1 bandwidth, *i.e.*, 10-20 GHz, not even matching up with the now far surpassed 2.5:1 TCA initial bandwidth. However, to improve on this operational bandwidth, a LC circuit can be introduced into the photodiode-to-antenna feed. By adding this extra circuitry, inductive lines enable implementation of a technique referred to as inductive peaking. Inductive peaking allows the antenna impedance to overcome the inherent capacitive nature of the MUTC photodiodes, flattening out the radiated power decay with a peak at a frequency tuned by the capacitive element of the LC circuit.

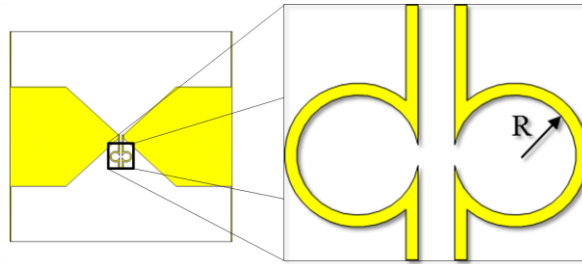


Figure 4.10: Inductive peaking RF current feed, R is the radius of the circles.

The new RF current feed design consists of a CPS with a partial circle interrupting the middle of each straight lines' path, as shown in Figure 4.10. These circular structures were introduced as a simple addition to the CPS lines to allow for maximization of inductance without changing the antenna unit cell size or shape. Sweeping different radii of the partial circle yielded a 5 GHz extension on the low end of the previous results to obtain a 4:1 (5-20 GHz) bandwidth, displayed in Figure 4.11.

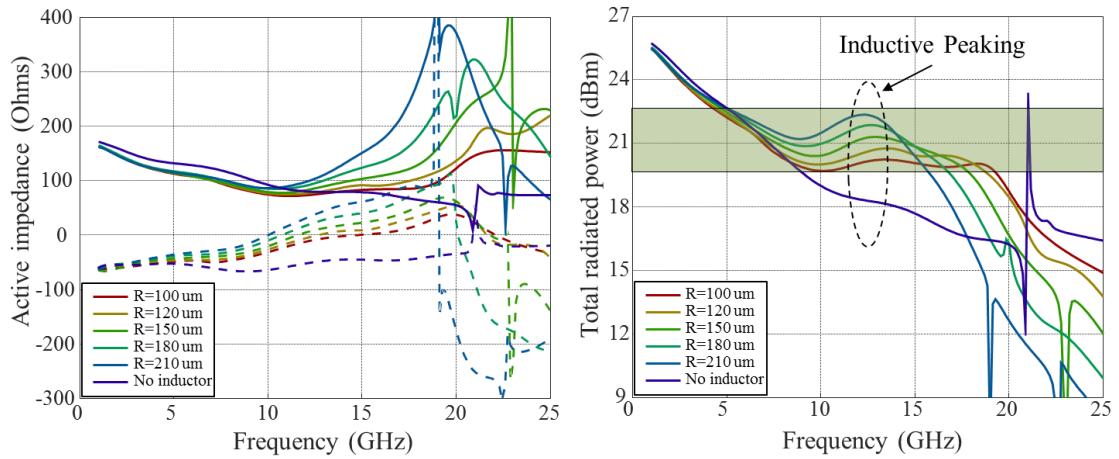


Figure 4.11: Effects of inductive peaking on active impedance, solid lines represent resistance and dotted represent reactance, and total radiate power at 70 mA photocurrent.

At low frequencies the substrate is electrically thin, causing the radiated power corresponding to the antenna impedance to become high. However, during operation it is expected the photodiode will readily saturate at these higher impedances due to the minimum biasing condition mentioned in section 4.1.2. Throughout mid-band operation, the inductive peaking adjusted impedance remains constant, with the photodiode responding accordingly, for a flat radiated response. Lastly, as higher frequencies are approached, integrated photodiodes aren't able to output sufficient RF power causing a sharp drop-off in antenna output power despite increasing antenna impedances.

4.2.2 Beam Steering

Upon completion of the CA model, a broad angular beam steering range, i.e. 0-45°, was simulated. Phase applied to the master and slave walls of the periodic boundary conditions in the infinite array model was determined using equation 3.3

based on the chosen steering angle. As the sweep from 0-45° was performed in the E and H plane, oscillations in the radiated power became more apparent as the steering angle approached 45°. Due to this characteristic, the approximate 4:1 bandwidth was only achievable with a steering angle up to 40°, as illustrated in Figure 4.12. Although this is not ideal, the photodiode-coupled CA accomplishes design goals of creating an UWB antenna with a broad steering range. Additionally, if the optical alignment system is correctly design, this antenna will also obtain the highly desired low-profile and conformal structures necessary for today’s applications.

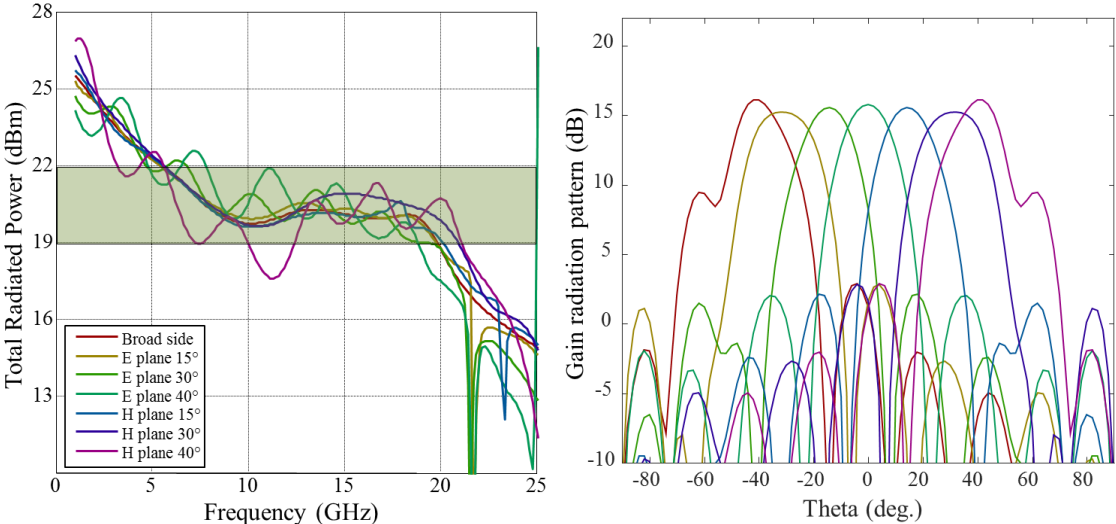


Figure 4.12: Simulated CA beam steering results at 70 mA photocurrent. The left graph shows the bandwidth of an infinite array, while the right shows the radiation pattern at different scan angles for a 12 GHz working frequency [44].

4.3 Discrete Photodiode-Coupled Array Antenna Modeling

Although the infinite array model is a convenient, computationally simple simulation method to maximize impedance bandwidth by editing the photodiode-coupled dipole unit cell, its accuracy diminishes with decreasing array size. As array size shrinks, finite array edge effects degrade antenna bandwidth. These effects are derived from an inability to uniformly excite the array due to reduced edge-element mutual coupling causing an active impedance imbalance between outer and inner unit cells. Thus, supplying each lumped port with equal power in attempt to reproduce uniform excitation will end in inner-outer element discrepancies, and narrowband impedance matching.

Simulation of these finite array edge effects is necessary to determine performance of the smaller array prototypes used to demonstrate beam-steering capabilities of an optical antenna fed Tx system. Accurate modeling of finite arrays can be accomplished by swapping the infinite array model's PBC on the planes truncating the dipole substrate with radiation BCs and extracting real and imaginary active S-parameters. Implementing both modeling parameters enables emulation of a finite antenna surrounded in free space while incorporating mutual coupling effects of each active element.

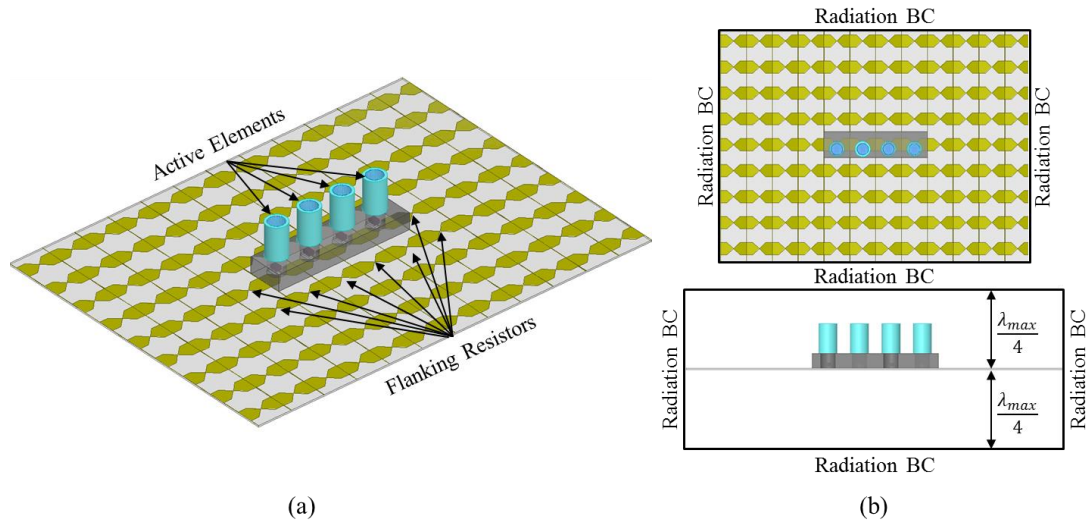


Figure 4.13: (a) 1 x 4 photodiode-coupled CA antenna with optical integration components, and (b) boundary conditions applied for finite modeling.

In order to sufficiently form and steer a beam, a 9 x 12 connected dipole array antenna surrounding a 1 x 4 active element photodiode-coupled CA array is proposed. This configuration model along with applied boundary conditions are illustrated in Figure 4.13 (a) and (b), respectively. Including “dummy” dipoles around the active array enables a potential to reduce finite array edge effects by adding in antenna impedance-matched flanking resistors at dipole inputs to extend RF current distribution outwards. Farther distribution of the RF current, rather than abrupt cut-off at the 1 x 4 edges, causes the active array to appear larger and approach the infinite array approximation. Additionally, finite array characteristic mode [41] resonances associated with the half-wavelength and wavelength of the array size in each direction can be shifted to lower frequencies outside of the operational bandwidth.

These characteristic mode related effects are illustrated in a dipole surface current distribution plot in Figure 4.14. In Figures 4.14 (a), (c), and (e), in which no

flanking resistors are present, the surface current distribution is strongly concentrated within the 1×4 lumped port excited dipoles allowing for potential bandwidth degrading characteristic mode resonances. Although there are traces of surface current in other dipoles, it is minimal incoherent excitation due to surface wave interacting with the surrounding dipole's metallic material. Contrarily, it can be seen in Figures 4.14 (b), (d), and (f) that the current distribution is uniformly spread in phase outwards for coupled-excitation of the surrounding dipoles for the appearance of a larger active element array. Further extension of the surface current is possible by simply extending resistor-populated dipoles outward for "larger" arrays.

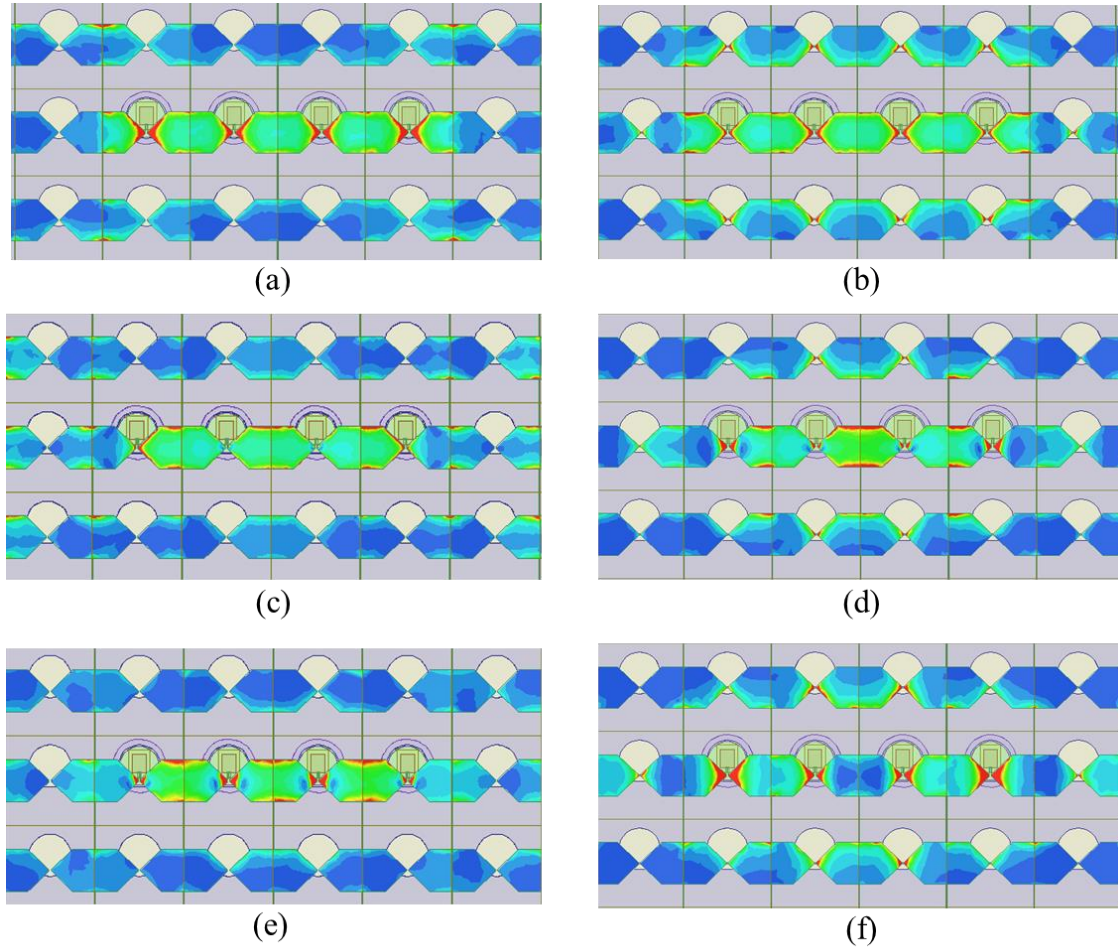


Figure 4.14: Surface current distribution for discrete 1 x 4 photodiode CA antenna model at (a) 5 GHz without flanking resistors (FR), (b) 5 GHz with surrounding FR, (c) 12 GHz w/o, (d) 12 GHz w/ FR, (e) 15 GHz w/o FR, and (f) 15 GHz w/ FR.

Implementation of the flanking resistors to shift the major characteristic mode resonances down towards $\sim 5\text{-}6$ GHz and below affords a 2.7:1 (6.5-17.5 GHz) bandwidth, as shown in Figure 4.15. Each photodiode within the model is assumed to operate at 70 mA up to 25 GHz, a moderate photocurrent for the $28\ \mu\text{m}$ MUTC photodiodes which remains consistent with previous infinite array simulations. As a

minimal array for beam steering operation, the simulation results presented in Figure 4.15 meet the requirements for a first generation design. Additionally, these results yield the lowest operational bandwidth in comparison to future, more populated arrays, *i.e.*, 8 x 8 arrays, setting a promising foundation.

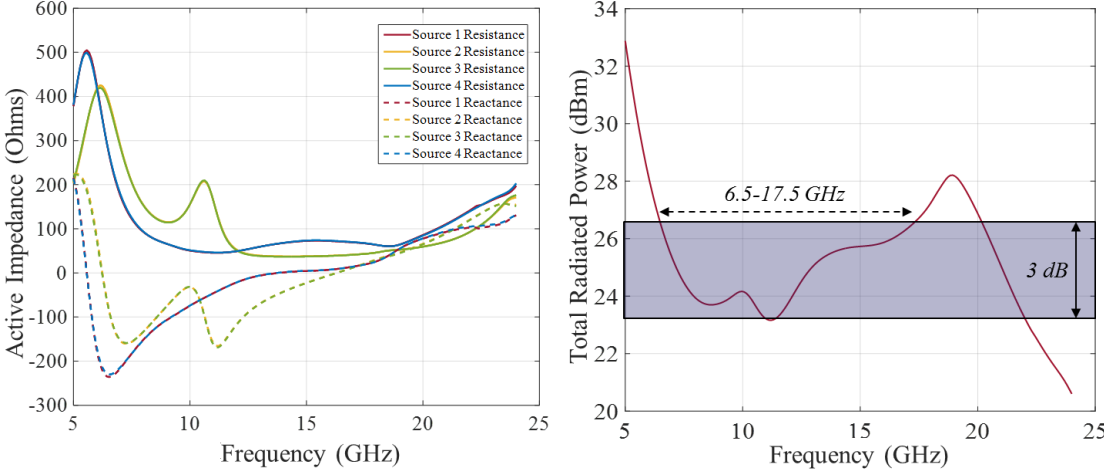


Figure 4.15: Active impedance and total radiated power of 1 x 4 CA antenna.

Chapter 5

FABRICATION AND OPTICAL INTEGRATION

The final CA design consists of gold dipole elements on a thin 250 μm AlN superstrate, which provides heat-sinking for the photodiodes. At the end of each dipole arm is a DC bias line and a 5 μm gap separating each unit cell for reverse biasing of the photodiodes. Initially, inductive peaking RF current feed lines connect to inner dipole ports were implemented to cancel out the inherent capacitive nature of the photodiodes; however, complications with photodiode integration eventually led to wire bonds to replace inductive peaking lines. The transition within the fabrication will be discussed in Section 5.2. This CA antenna design is fabricated in parallel with MUTC photodiodes and AlN sub-mounts used for wire bonding. After fabrication, fiber alignment spacer/mounts are designed and printed to link the photodiode-coupled antenna to all optical feed components, *i.e.*, GRIN lens, fiber ferrule, and mating sleeve purchased from Thorlabs, Inc. The entire fabrication and optical integration process is briefly overviewed in Figure 5.1, and discussed more in depth throughout the remaining sections.

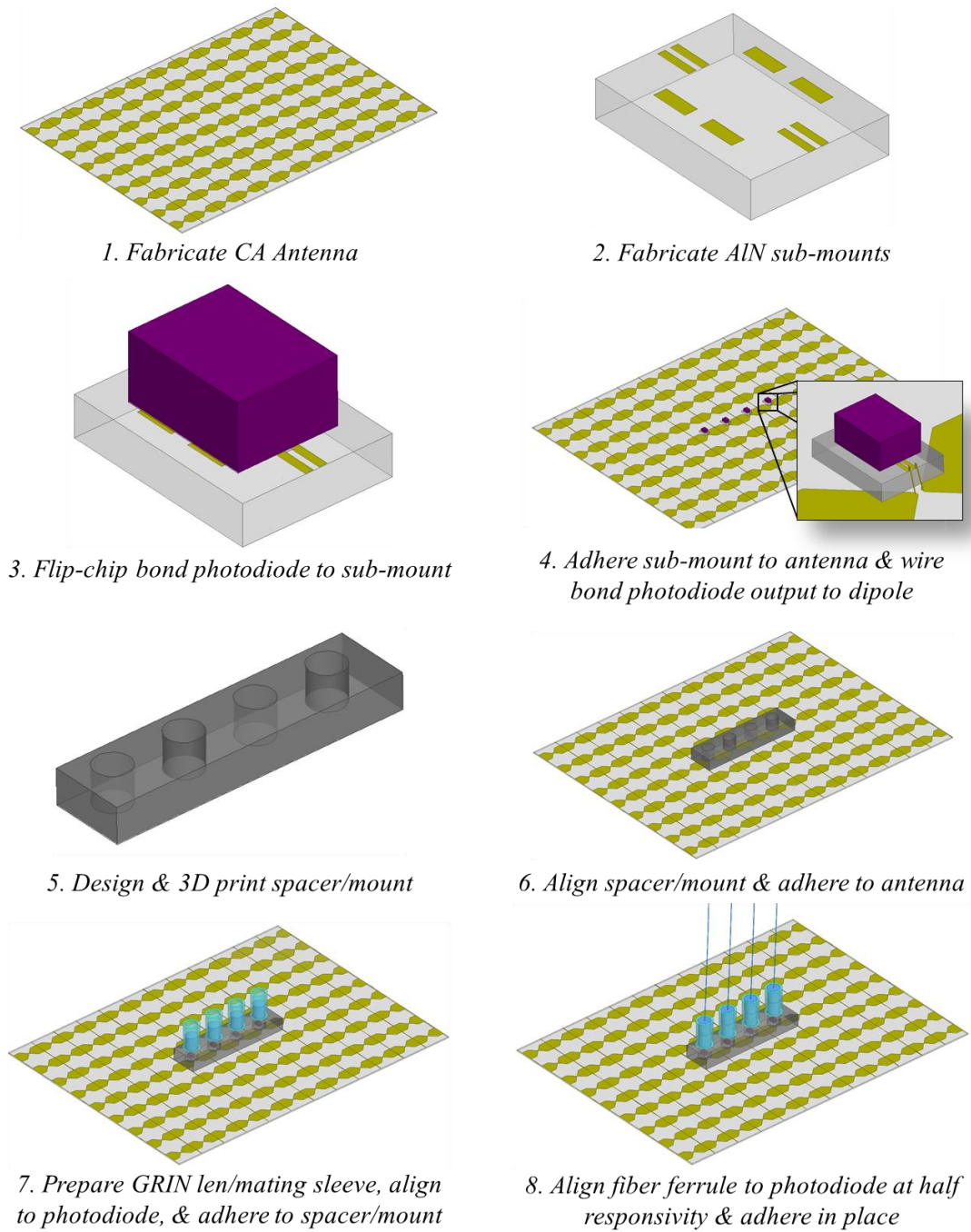


Figure 5.1: Overview of 1 x 4 photodiode-coupled CA antenna with integration of optical components linked to feed network.

5.1 Antenna

The fabrication process starts with a pre-deposition cleaning of the AlN used as the antenna substrate. Storage of AlN allows for accumulation of organic contaminants on the surface of each substrate, removal of these contaminants is necessary for uniform thin film depositions free of non-intrinsic adhesion issues. To accomplish this, a 10 minute oxygen plasma clean is performed to provide a pristine surface for deposition of gold (Au) forming the antenna elements. One issue with deposition of Au onto the CA antenna substrates is it doesn't readily adhere to AlN. In order to enhance adhesion, a seed layer of titanium (Ti) is first deposited to act as a glue-like layer allowing Au to be subsequently deposited. Since each material is common and step coverage is not an issue, deposition of the 20 nm Ti and 50 nm Au seed layer was performed using evaporation.

Next, the CA of dipoles needs to be patterned. A photomask consisting of a 12 x 9 array of dipole elements connected to a bias control port was designed to accommodate active arrays up to 8 x 8 with a current distribution dissipation area of non-active elements around the edge. Prior to using the mask, a negative photoresist needs to be deposited onto the TiAu-coated AlN substrate. NR2-8000P (Futurrex, Inc., Franklin, NJ) was selected as the negative photoresist due to requirement of resolving mask pattern negative, and high viscosity properties enabling thick layers to be formed making it possible to develop thick enough Au dipoles to satisfy the skin depth relation. Since NR2-8000P is so viscous, it can't be readily filtered through the standard 0.2 μm pore size filters utilized to ensure a contaminant and defect free resist is deposited over large substrate areas like the CA antenna. Therefore, a pressure-driven filtering apparatus was constructed, shown in Figure 5.2, to filter pure NR2-8000P, and other viscous materials, prior to spin deposition. Filtered NR2-8000P is

then spun at 4000 rpm for 45 seconds, and soft baked at 150°C for 60 seconds to settle a uniform layer ready for photolithography.

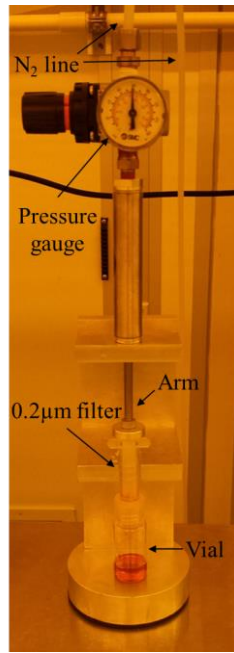


Figure 5.2: Pressure-driven filtering apparatus used for NR2-8000P filtration.

The photolithography process begins with alignment of the substrate and 12 x 9 CA antenna pattern, after which the sample is brought into contact with the mask until stable fringe patterns are visible. The exposure dose used was 400 mJ/cm² at 365 nm (i-line). Post-exposure, removal of the sample from the mask aligner should be done slowly as the NR2-8000P often sticks to the mask resulting in the photoresist tearing away from the sample. Upon removal of the sample, a post-bake is done at 80°C for 60 seconds to activate the negative resist properties. Unexposed NR2-8000P will then be removed during the subsequent 60 second lightly-agitated development in

RD6 developer followed by another 60 second rinse under de-ionized (DI) water. Finally, the sample is dried off using N₂ and is ready for Au electroplating.

Electroplating is accomplished using Techni-Gold 25 ES TRU solution (Technic) to grow a 3 μm thick Au CA antenna. NR2-8000P was first removed from each corner with acetone to open up connection ports for the current source's anode at the Au seed layer. Upon secure physical and electrical connection of the CA antenna substrate, it is immersed in Au solution where a cathode-linked conductive plate resides. An electrical current is induced, flowing from the conductive plate to the antenna substrate, simultaneously carrying Au⁺ ions to Au regions exposed from photolithography until accumulation of a 3 μm film.

The final fabrication step is a multi-etch removal of resist and TiAu seed layer to fully resolve the CA pattern. First, the NR2-8000P is removed using a chemical mixture of sulfuric acid (H₂SO₄) and hydrogen peroxide (H₂O₂), 3:1, commonly referred to as piranha. A subsequent DI water rinse follows prior to submerging the substrate into Au etch to remove the Au portion of the seed layer. Again, the CA antenna should be rinsed in DI water before being placed back into piranha for etching of the Ti seed layer. It is important to make sure all of the piranha solution is thoroughly rinsed before exposing the substrate to the iodine Au etch, or vice versa. As a strong oxidizing agent, piranha will initiate a violent chemical reaction if exposed to iodine. One final DI rinse and N₂ dry step results in an exposed AlN layer ready for edge dicing to remove residual material on corners from electroplating. The completed CA antenna is pictured in Figure 5.3 with focus points on both the 5 μm DC bias-block gap, and the bonding pads designed for gold-gold thermo-compression flip-chip bonding.

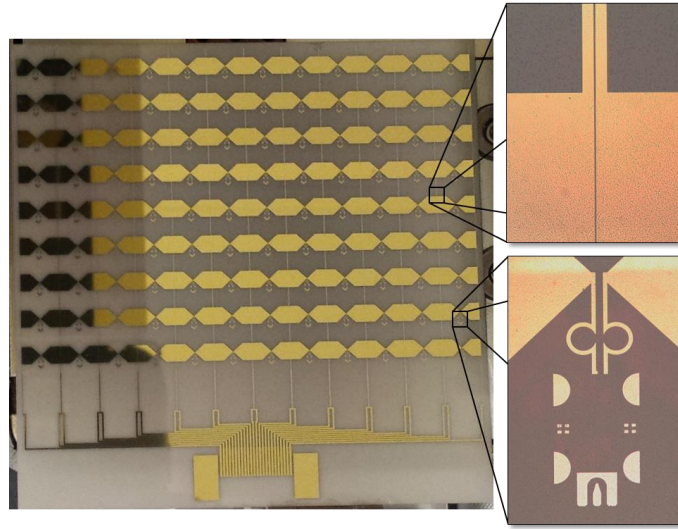


Figure 5.3: Fabricated CA antenna with biasing feed network connection port, 5 μm DC bias-block gap (top right), and photodiode bond pads (bottom right).

5.2 Photodiode Integration

Initially, photodiode integration into the CA antenna substrate consisted of standard gold-gold thermo-compression flip-chip bonding with added ultra-sonic tip movement. Ultra-sonic capabilities have aided in breaking the gold-gold grain boundary formed during photodiode test bonding to AlN sub-mounts for reduction of device dark current. Using this technique proved successful for single direct antenna photodiode integration; however, attempting to bond multiple photodiodes on the same antenna substrate resulted in constant misalignment, shorting, or disconnection of previously bonded photodiodes. Essentially, a gold-reflow was induced during the thermal cycling of the flip-chip bonding stage when a second photodiode was compressed into the antenna substrate; this gold-reflow combined with thermal expansion induced stress resulted in the precisely bonded 28 μm photodiodes without

applied bond pressure to become shorted or disconnected. Mis-alignment shifts did not occur every single bonding cycle allowing re-bonding in an effort to obtain a 1 x 4 photodiode array. However, re-bonding either diminished bond strength as indentations from previous attempts limited connection points, shown in Figure 5.4, or was not possible due to gold bond pad detachment from the indium phosphide (InP) photodiode chip. Additionally, the thin 250 μm AlN CA antenna substrate experienced “warping” during 300°C to room temperature cooling on the stage leading to disconnection of bonded photodiodes.



Figure 5.4: Post-disconnection photodiode bond pad with resultant indentations.

To circumvent issues experienced in multi-photodiode thermo-compression flip-chip bonding, conventional photodiode-to-sub-mount flip-chip bonding was followed by thermal epoxy adhesion of the sub-mount to the CA antenna substrate and wire bond electrical connection of sub-mount to dipoles. This new process change was input into the previous HFSS models and optimized for matching radiation performance. By matching the inductance of the original CPS RF feed lines to new 0.75 mil air-bridge wire bonds, the antenna performance was not altered.

Although the photodiode integration approach changed, re-design and fabrication of the 12 x 9 CA antenna substrate was not necessary. A laser ablation technique enabled removal of inductive peaking RF CPS line's electrical connection to four adjacent dipoles. Incorporation of the technique was also included in the simulation results and did not alter antenna performance either. After laser ablating the original RF current feeds, four operational photodiode/sub-mount units were aligned to the inner dipole ports, and adhered using low viscosity, thermally conductive epoxy (KONA 870FT-LV-DP, Resin Technology Group, LLC). Once cured in place, the CPW output on the photodiode sub-mount was wire-bonded to the appropriate dipole arms, as highlighted in Figure 5.5. In order to ensure a reliable wire bond link from the photodiode to antenna during any jostling or substrate flexion, epoxy was applied around each sub-mount to encase all wire-bonds. This robust epoxy-based securing technique was also used on the flexible flat cable (FFC) bias feed connector soldered to the CA antenna bias port.

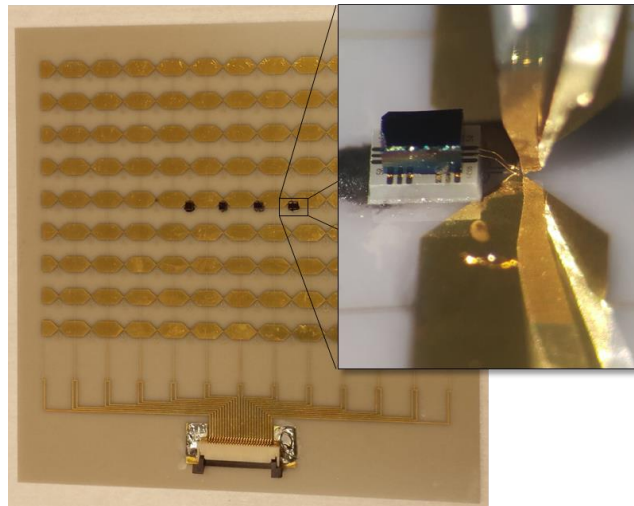


Figure 5.5: Four photodiodes thermally and electrically connected to CA antenna.

The FFC input into the connector on the CA antenna will be supplied by a DC biasing board capable of being controlled manually or electronically. Manual operation increases simplicity for initial photodiode testing, *i.e.*, IV curve characterization, and acts as a current link for optical fiber alignment to be discussed in Section 5.3.3. Electronic control via FET relays provides more agile tuning during full beam steering where all aspects of antenna can be traced to a single software program. The 1 x 4 populated photodiode biasing control board is presented in Figure 5.6.

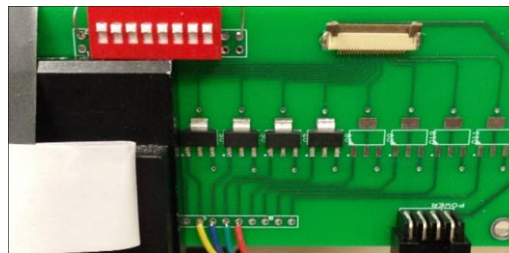


Figure 5.6: Bias control board used for DC reverse-bias supply to photodiodes, and as a current link for reading optical alignment currents.

5.3 Coupling Photodiodes to Optical Feed Network

With the photodiodes strongly secured to the CA antenna both electrically and thermally, along with a method of accurately reading photocurrent, coupling a single-mode fiber to the photodiode can be accomplished. The optical alignment consists of 3 primary steps: (1) design, print and align fiber spacer/mount, (2) assemble GRIN lens/mating sleeve unit, and (3) align light to photodiode and secure fiber, GRIN lens, mating sleeve, and fiber spacer/mount together.

5.3.1 Spacer/Mount Preparation

As mentioned in Section 3.2.1.4, the fiber spacer/mount should be designed with a permittivity value as close to free-space, minimizing back-radiation towards the optical feed network. Rather than risk structural stability by removing sections of the body, the full, 25 mm x 25 mm x 6 mm, design resembling spacer 1 can be 3D printed using a low fill-factor to reach permittivity values of ~ 1.1 . Four sets of circular slots are spaced 6.35 mm apart to align over each of the photodiodes; the slots consist of a circle of radius, $r_1 = 1.3$ mm, extending up 3 mm from the bottom, and a circle of radius, $r_2 = 1.9$ mm, extending down 3 mm from the top side. At the merging point, a ledge forms a set point for the GRIN lens/mating sleeve unit to stabilize for alignment, as shown in Figure 5.7 (a). After printing, a 12 mm x 24.5 mm x 2 mm section was removed from the underside for positioning tolerance, and clearance of all four photodiodes on sub-mounts during spacer/mount setting. The finalized spacer, complete with clearance opening can be seen in Figure 5.7 (b).

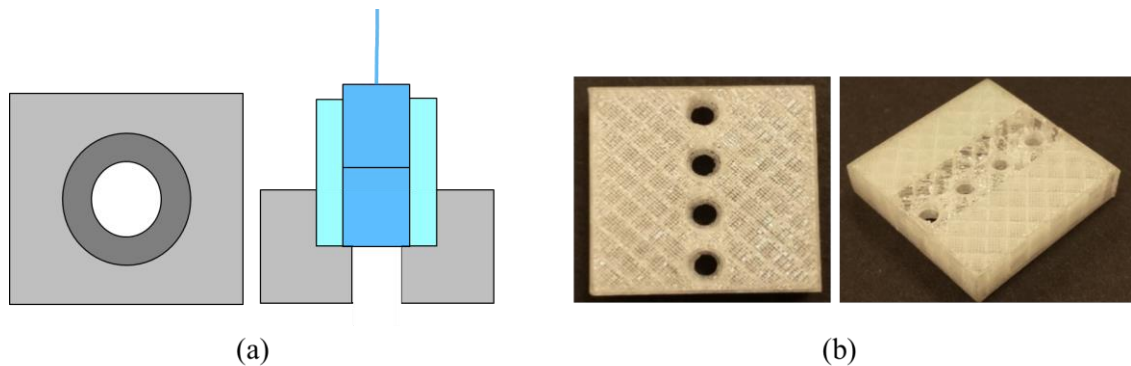


Figure 5.7: (a) Schematic of GRIN lens/sleeve/fiber unit set on spacer/mount ledge and (b) 3D printed fiber spacer/mount used for 1 x 4 CA antenna.

5.3.2 GRIN Lens/Mating Sleeve Unit Preparation

Preparation of the GRIN lens/mating sleeve unit is relatively simple. First, NOA 61 (Norland Products), a UV-curable optical adhesive, should be lightly applied to the curved outside of the GRIN lens cylinder. Applying too much optical adhesive can cause dispersion onto the flat edges potentially interfering with the light path, setting of the sleeve into the spacer/mount, or blocking the fiber ferrule path into sleeve. Next, the GRIN lens is slid into the matching sleeve until the flat ends of the GRIN lens sit flush. The unit is subsequently UV cured, then ready for optical alignment.

5.3.3 Optical Alignment

Optical alignment begins with mounting the antenna substrate containing the four photodiodes, and FFC connector onto a vacuum stage with six degrees of movement freedom. The GRIN lens/mating sleeve unit is set into a 3D-printed clamp positioned over the photodiode currently being aligned. A fiber feed clamp, connected to a separate stage, resides over the sleeve clamp to input the fiber ferrule into the sleeve while retaining the ability to control focal point position by sliding the ferrule up and down. Finally, a FFC links the connector on the antenna to the bias control board enabling read-out of the DC photocurrent produced during optical-coupling to the photodiode.

Placement of the spacer/mount needs to be done with precision to ensure light from each slot can be coupled to its respected photodiode. Before alignment, the base of the spacer is evenly coated in UV-curable optical adhesive, NOA 61. Rough positioning over the photodiodes is accomplished by hand, followed by fine tuning with stage translation under the GRIN lens/mating sleeve. Once max responsivity of

each photodiode can be read with the sleeve set at the base of the spacer, the spacer is cured under UV exposure for 2 minutes. At this point the spacer should be firmly in place; however, additional NOA 61 is applied and cured around the outer edge for a more reliable bond to hold against potential strain once the fibers are connected.

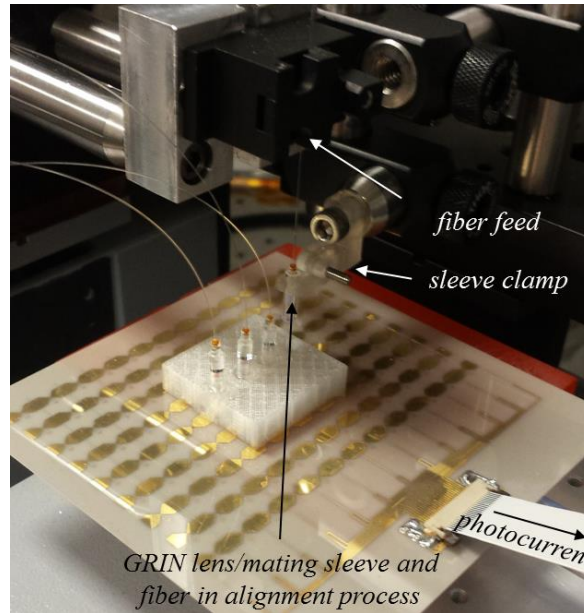


Figure 5.8: Optical integration set-up during alignment of fourth element.

With the spacer in place, the GRIN lens/mating sleeve unit is reintroduced with the fiber ferrule into the spacer slots. Stage translation scanning for local maximum current, indicating max responsivity, through focal point positioning on the photodiode junction determines the location of the GRIN lens/mating sleeve at the ledge of the spacer slot. While holding this local maximum reading, NOA 61 is applied around the sleeve, completely filling vacant slot space, to secure an accurate focus on the $28\ \mu\text{m}$ photodiode. Curing this epoxy dose requires more precision than a

standard flood UV exposure; therefore, two UV fiber-light “wands” are used to uniformly cure the optical adhesive over time in attempt of eliminating uneven solid/liquid NOA 61 barriers causing sleeve and alignment shifting.

Lastly, focal point selection along the axis passing normal through the photodiode’s junction is selected by translating the fiber ferrule up and down within the sleeve. Maintaining consistent with the common power handling theme of the MUTC photodiodes, positioning of the ferrule resolves a focal point off-set from the photodiode. By translating the focal point, MUTC photodiodes are able to operate at higher maximum output power at half-maximum responsivity by uniformly illuminating the entire junction to reduce the peak to average optical power across the photodiode. Upon reaching half-max responsivity the ferrule is cured to the inside of the sleeve.

After performing the same process three more times for each GRIN lens/mating sleeve unit and fiber ferrule, the optical alignment is complete. Before removing the optically-coupled CA antenna from the vacuum stage, final responsivity measurements are recorded determining overall success. Responsivities recorded for each photodiode are present in Table 5.1, where numbers 1-4 correspond to left to right positioning displayed in Figure 5.9.

	PD #1	PD #2	PD #3	PD#4
Initial max \mathfrak{R} (A/W)	0.70	0.70	0.74	0.70
Packaged \mathfrak{R} (A/W)	0.26	0.29	0.32	0.20

Table 5.1: Comparison of photodiode responsivity before and after optical alignment.

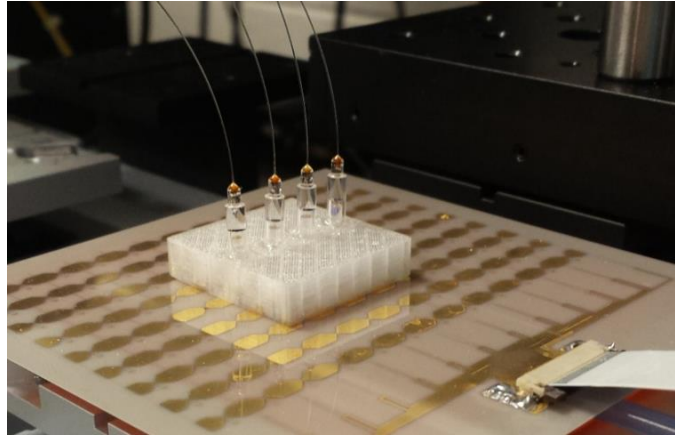


Figure 5.9: Successful integration of 4 single-mode optical fibers to MUTC photodiode-coupled CA antenna [44].

Based on the large discrepancies (<75%) between expected packaging responsivities, *i.e.* PD #1: 0.35, PD #2: 0.35, PD #3: 0.37, and PD #4: 0.35, the optical alignment process needs to be refined in order for ideal responsivity packaging to be maintained over time. Primarily, error in integration stems from the uneven curing between the sleeve and fiber/mount slot inner wall. Although responsivity drift is minimized by balanced curing from the UV “wands,” adhesive hardening is capable of exerting undetected forces on the GRIN lens/mating sleeve due to the sleeve clamp’s temporary support. Removal of the sleeve clamp eliminates cancellation of these forces, allowing the GRIN lens/mating sleeve to physically move, resulting in an optical shift off of the 28 μm diameter target. Additionally, factoring in tugging on optical fibers, spacer slipping during curing, and hardened optical adhesive obstructions within the sleeve multiplex potential inaccuracies into a complex and delicate process, diminishing physical tolerances and room for error. If one or two of these issues, most likely spacer/mount slot size and placement accuracy, become

avoidable the presented optical integration will routinely provide accurate coupling at half, max responsivity.

5.4 Packaging

After aligning 4 input fibers to 4 wire bonded photodiodes, the $7.5 \times 7.5 \text{ cm}^2$ antenna substrate requires a protective housing for characterization and transport. Similar to the spacer/mount, the protective, low fill-factor housing was 3D printed into a hollow $16.5 \times 12.5 \times 6.5 \text{ cm}^3$ ABS box with a $5.5 \times 7.5 \text{ cm}^2$ rectangular slot opening for undisturbed antenna radiation. Enclosing the open backside is a $16.5 \times 25 \text{ cm}^2$ Plexiglas sheet extended down from the antenna housing to enable mounting of biasing control and optical fiber adapters underneath. DC bias control connection is accomplished by feeding a FCC through a rectangular slot in the bottom of the housing. Connection to the optical phase feed network is realized in the same manner, followed by securing each fiber into adaptors matching each photodiode's respected feed channel. Additionally, $\frac{1}{4}$ -20 tapped holes in the underside of the protective housing serve as structural links to testing fixtures for characterization. All details commented on are highlighted in Figure 5.10.

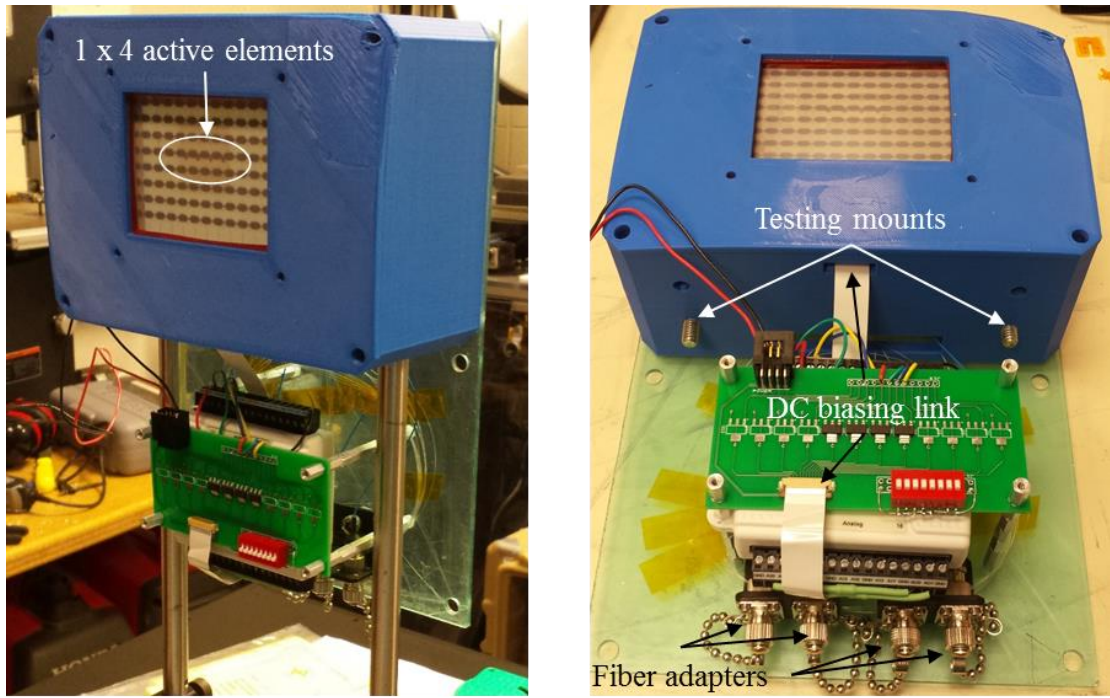


Figure 5.10: Packaged photodiode-coupled CA antenna with mounted biasing board.

Chapter 6

TX SYSTEM CHARACTERIZATION

6.1 System Architecture

The UWB photonic phased array TX system is comprised of the UWB tunable photonic RF source and phase control feed network, discussed in Chapter 3, as the backend while the 1 x 4 photodiode-coupled CA antenna presented in Chapter 5 forms the architecture's frontend. A computer loaded with LabVIEW is responsible for electronic control of the tunable source signal, phasing each channel input into the CA antenna, and data acquisition extracted from an electronic spectrum analyzer connected to a horn receiver. Figure 6.1 illustrates the connection of each sub-system with annotation of specific connection types.

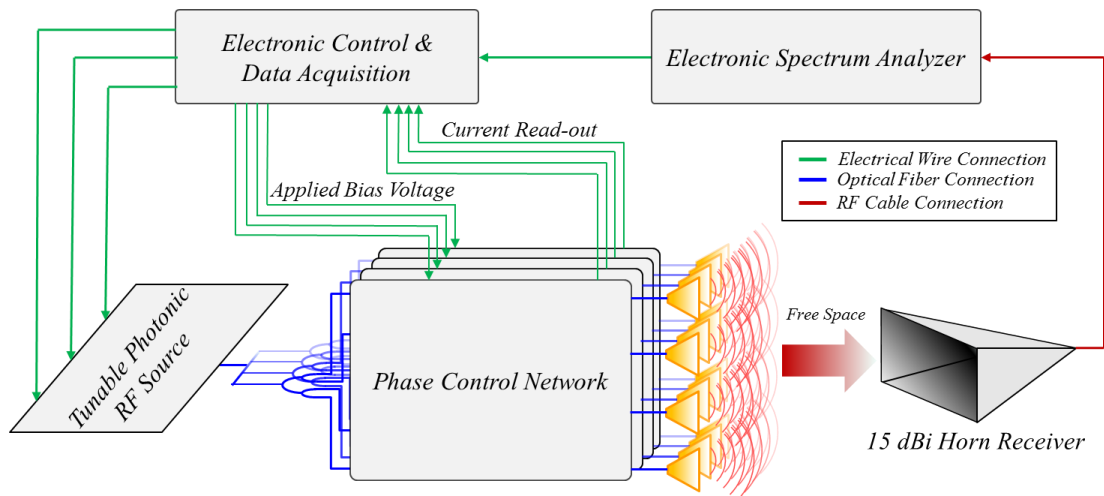


Figure 6.1: Tx system architecture including UWB tunable photonic RF source, phase control network, CA antenna, and data analysis and control equipment.

The UWB tunable RF source is realized by assembling two distributed feedback (DFB) lasers, laser diode driver, thermo-electric cooler (TEC), a high-speed EO modulator, PM optical fibers, optical semiconductor amplifier, and EDFA into a rack mount, as depicted in Figure 6.2. Connection of an Agilent PSG source provides the LO signal modulated onto the master DFB laser for injection locking of the DFB slave laser. Each DFB laser provides up to 10 dBm of output power operating at ~1550 nm. Parametric adjustments in the Tx system LabVIEW program enables continuous tuning of CA antenna operation bandwidth of 4 – 20 GHz and beyond through use of 1 – 3 harmonic locking of a <10 GHz LO modulated signal. Fine tuning of the TEC via a laser diode driver, also controlled by LabVIEW, enables accurate and reliable phase locking due to circumventing of external temperature influence on the laser sources.

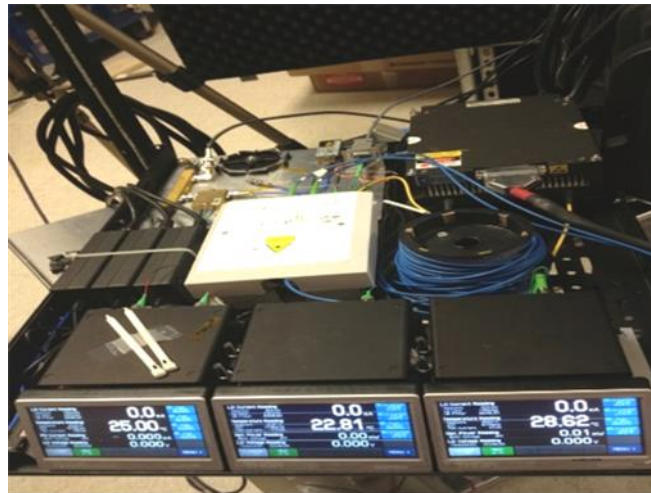


Figure 6.2: Tunable photonic RF source installed into a rack mount [42].

The optical phase feed network is assembled into a separate rack mount, as shown in Figure 6.3, consisting of an optical fiber coupler, 45° rotation key, optical fiber splitters (into 4 channels), 4 EO phase modulators, and 4 linear polarizers linked to single-mode fiber outputs. Two optical fiber inputs from the tunable photonic RF source seen in the bottom left of Figure 6.3 are combined into one PM fiber before being split into 4 channels. Each channel is then coupled into an EO phase modulator. Control of modulator biasing for beam steering is accomplished through the same Tx system LabVIEW program used for the source. Voltage signals are controlled by the LabVIEW program and applied via a National Instruments' Digital Acquisition (DAQ) to the EO phase modulators. Modulation voltage signals input after determining values through equation 3.3 and an automatic phase calibration routine to measure channel pairs' phase. The phase calibration is accomplished by sweeping the phase front of one reference channeled paired separately with three variable channels switched on and off by a separate DAQ voltage signal controlling field-effect-transistor (FET) switches. Due to path length mismatch, and use of phase modulators instead of a true time delay (TTD), calibration is repeated at each chosen frequency before modulation voltage application and signal output through the four fiber channels (lower left of Figure 6.3) into the CA antenna for beam steering demonstration at each respective frequency.

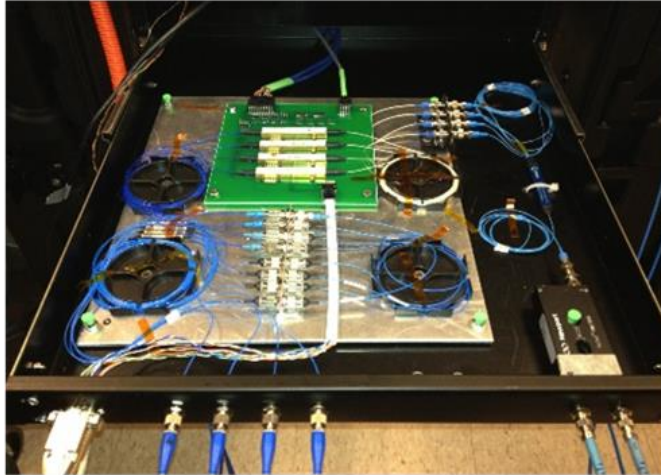


Figure 6.3: Optical phase control network assembled in rack mount [42].

Beam steering demonstrated by the 1 x 4 CA antenna is subsequently captured by a 15 dBi horn receive antenna, placed in the far-field region ($d_{Rx} \approx 10\lambda_{max} = 75 \text{ cm}$), and output through a 2.4 mm RF coaxial cable to an electronic spectrum analyzer (ESA), illustrated in Figure 6.4. During antenna operation, the bias control board is linked to a Keithley SourceMeter for PD bias control and current read-out, along with DAQ for channel operation selection (used in phase calibration). All of this information is interfaced with the CA through a FFC concurrently.

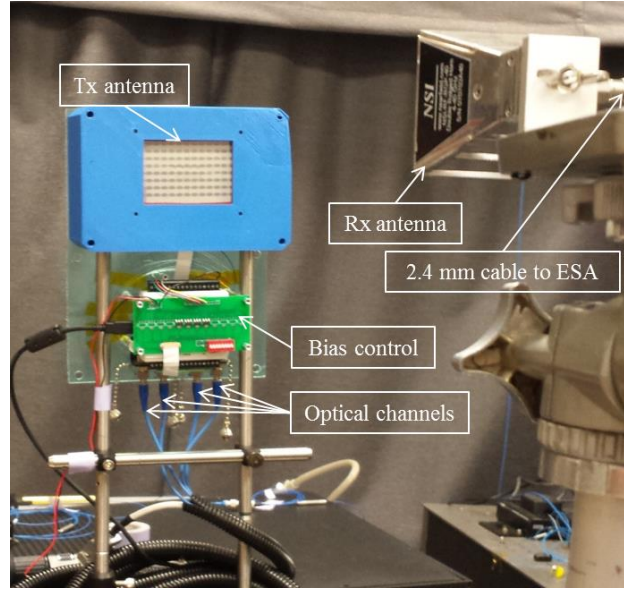


Figure 6.4: 1x4 active element CA antenna radiating into the fair-field to a horn receive antenna connected to an ESA by a 2.4 mm RF cable.

6.2 Characterization and Results

Characterization of the 1x4 photodiode-coupled CA antenna is accomplished by recording time-stamped beam steering radiated power profiles cycled from -90° to $+90^\circ$, over a period of 400 ms, at incremental frequencies swept from 4-24 GHz. After recording the radiated power steering profiles, the broadside radiation at each frequency is extracted for separate effective radiated power (ERP) calculations. In order to obtain an accurate ERP value at each frequency, all of the loss within the Tx system must be compensated for. Implementing Friis' transmission equation to acquire ERP provides the best approximation of the power transmitted by an antenna,

$$ERP [dBm] = P_r - G_r - L = P_t + G_t, \quad (6.1)$$

where P_r is the power received, G_r is the gain of the receiver, L is the free space path loss, P_t is the power transmitted, and G_t is the gain of the transmitter. An exact

calculation of transmitted power is not trivial due to the unknown Tx antenna gain. Therefore, the 1 x 4 photodiode-coupled CA antenna's transmitted gain and power are combined into the presented ERP.

Unfortunately preliminary low power tested resulted in one of the four photodiodes becoming shorted due to suspicious high dark current values. Although not ideal, the remaining 1 x 3 continued through ERP and beam steering characterization. Figure 6.5 presents the ERP of the 1 x 3 operating at 60 mA and at 90 mA total photocurrent input, 20 mA and 30 mA from each photodiode, respectively. The data presented here accounts for the free space path loss (FSPL), gain between the transmit array and receiving horn antenna, and cable loss between the receive antenna and spectrum analyzer. At 60 mA the bandwidth is slightly less than 1 x 3 simulation results; however, the ~5 dBm offset curve shapes are nearly identical. As the MUTC photodiodes are driven to higher current values, *i.e.*, 90 mA, the photodiode bandwidth increases to extend and flatten out the CA antenna frequency response towards the goal of a 4:1 (5-20 GHz) bandwidth.

In each case, the effective radiated power is ~5 dBm down from ideal simulated radiated power results. This discrepancy is primarily contributed by master/slave laser power imbalance causing an unequal two tone optical signal, *i.e.*, $P_{opt1} \neq P_{opt2}$. By having an unbalanced two tone optical signal launched through the optical phase feed network, the modulation depth of the signal is decreased. Therefore, the effective radiated power transmitted from the photodiode-coupled CA antenna is decreased by the power relation, $P_{ideal} = \frac{1}{2} M_{\omega}^2 I_{pd}^2 R_L$, where M_{ω} is the modulation depth. Once the lasers are sufficiently balanced and photodiodes are driven to higher

currents, ERP values will drastically increase with flat responses matching simulation results.

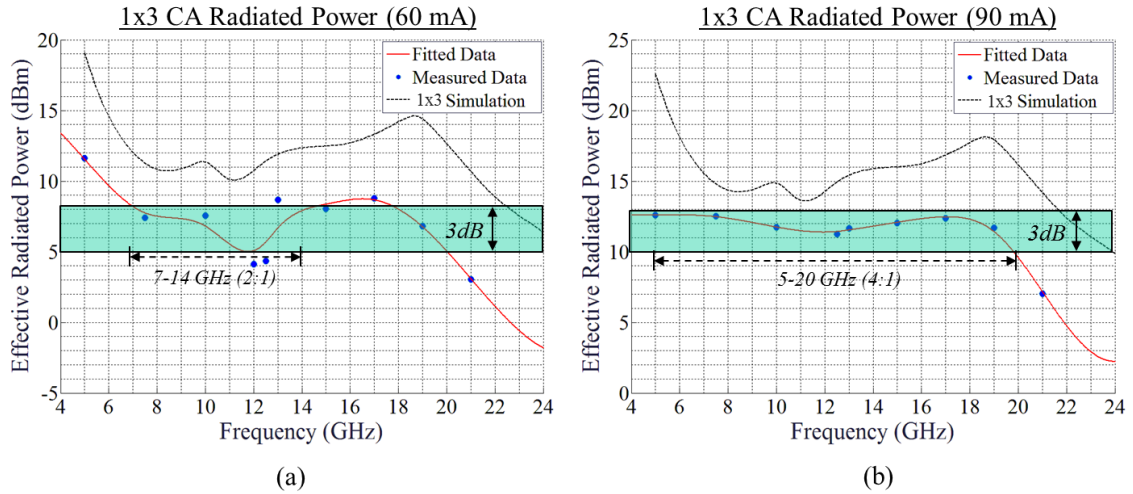


Figure 6.5: Effective radiate power demonstrated by 1 x 3 photodiode-coupled CA antenna at (a) 60 mA and (b) 90 mA.

As mentioned, the ERP data is formulated by extracting broadside radiated power values and compensating for FSPL, receiver gain, and cable losses from raw beam steering data. In order to present the beam steering capabilities of the 1 x 3 photodiode-coupled CA antenna, a time-stamped plot of -90° to $+90^\circ$ cyclic beam steering at an operating frequency 15 GHz is included in Figure 6.6. Troughs exemplify -90° and $+90^\circ$ steering angles positioning the radiated beam as far away from the stationary broadside horn receive antenna as possible, minimizing received radiated power. Alternatively, the peak represents a broadside beam directed at the horn receiver for maximized radiated power reception. Measuring between these peaks

and troughs, an extinction ratio as high as 34 dBm is achieved, yielding efficient beam steering capability with side lobe suppression.

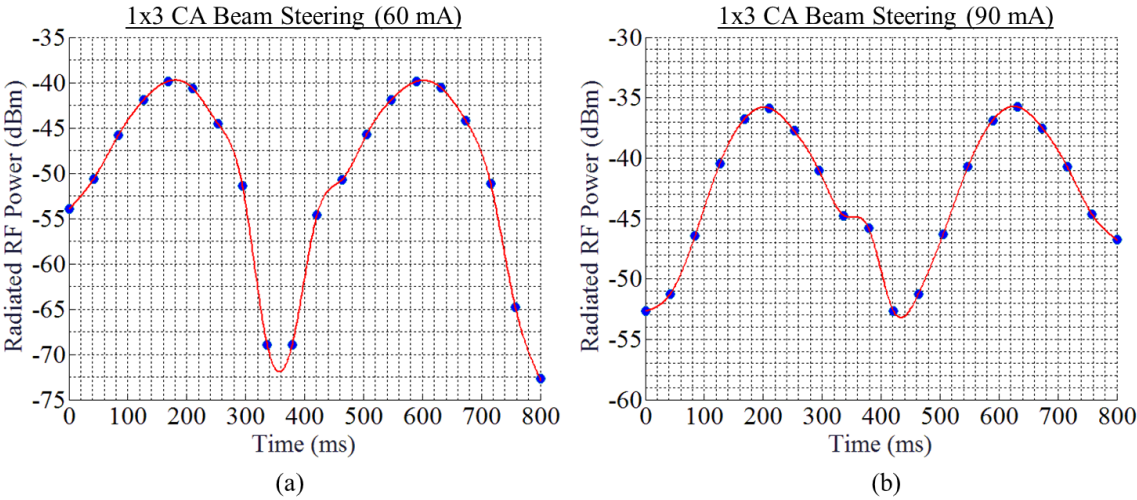


Figure 6.6: Time-stamped plot of two periods of -90° to $+90^\circ$ beam steering at an operating frequency 15 GHz for (a) 60 mA photocurrent operation and (b) 90 mA photocurrent operation. The troughs represent -90° and $+90^\circ$ directions and peaks represent broadside displaying an extinction ratio of 34 dBm at 60 mA and 19 dBm at 90 mA.

Chapter 7

CONCLUSION

7.1 Summary

An optical approach to driving an infinite current sheet, realized here as a connected array, was shown to address many of the challenges associated with electrical feeding. In doing so, state-of-the-art integrated photodiodes developed at UVA and a novel optical feed network developed at University of Delaware were used. Initial design of a simple connected array antenna indicated a relative bandwidth of 4:1 while potentially outputting up to 25 dBm of RF output power per element using MUTC photodiodes. Preliminary low-power 1x4 array bandwidth data demonstrated good agreement with simulations. High fidelity beam steering was also demonstrated over the array's operational bandwidth.

7.2 Future Work

Future progression of this research will focus on a multiple improvements to evolve the current 1 x 4 prototype into a system capable of integration into avionic platforms while meeting AESA requirements. First, optical integration will transition into a low-profile architecture. By coupling optical fibers to the photodiodes at an input parallel to the CA antenna substrate the antenna's profile can be significantly reduced. To accomplish this, 2 mm prisms will redirect the two-tone optical signal 90° onto the 28 μm photodiode to enable equally efficient optical alignment while reducing the CA antenna thickness to ~4 mm. This new optical alignment approach also allows for implementation of a ground plane behind the CA substrate, not

previously possible due to fiber bending radius restriction on thickness, for more efficient radiation performance.

Second, more complex modulation techniques, namely quadrature amplitude modulation (QAM), are to be implemented to demonstrate data transmission capabilities. Both the low-profile optical integration and QAM demonstration will be included in the next generation 1 x 8 photodiode-coupled CA antenna design presented in Figure 7.1. For this new design, optical alignment will follow similar process flow with the only difference being a prism will be secured in alignment with the photodiodes before aligning the GRIN lens/sleeve/optical fiber ferrule unit. QAM implementation will be integrated on the backend of the system by coupling modulators capable of QAM into each channel of the phase feed network. Initially, QAM transmission with beam steering performance will be limited to a narrow instantaneous bandwidth and less than ideal efficiency until phase modulator phase shifters are replaced with true time delays (TTD). Furthermore, UWB TTD should be integrated to expand the data transmission instantaneous bandwidth towards the UWB operational bandwidth.

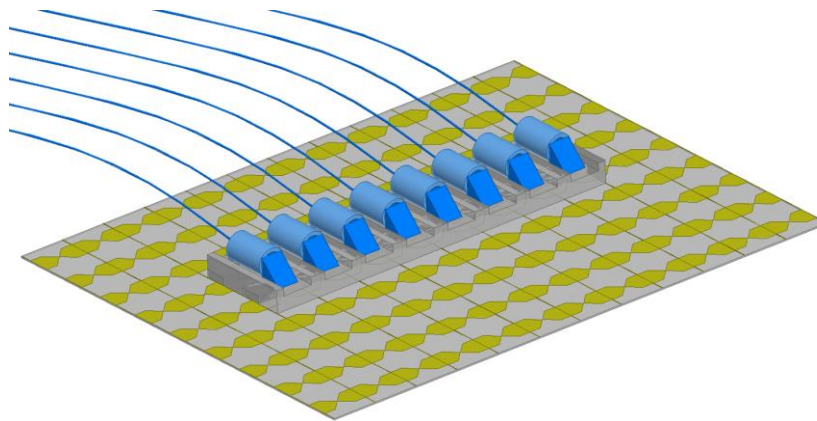


Figure 7.1: Proposed low-profile 1 x 8 photodiode-coupled CA antenna design.

Post-second generation design focus will be on scalability of the optical integration to approach the 10 x 10 active element operation for close infinite CSA performance matching. Scalability processing provides many advantages to the communication applications. Larger array size capabilities paired with optical fiber feeds enabling dense population can be utilized to create more unique, layered aperture layouts capable of increasing operational bandwidth and forming narrower beams [43]. Additionally, these wideband array concept advantages can be exploited through multiple-input multiple-output (MIMO) operation to increase transmitting capacity by spatial multiplexing Tx data. Incorporation of all these new design considerations provides a promising path towards accomplishing UWB mm-wave multi-functionality with a low profile, low SWaP+C single aperture that has not yet been possible through electrical excitation techniques.

REFERENCES

- [1] D. W. Corman, P. Moosbrugger, and G. M. Rebeiz, "The Industry's Next Tipping Point," *Microwave Journal*, vol.57, no. 5, pp. 26–38, 2014.
- [2] C. Hemmi, R. T. Dover, F. German, and A. Vespa, "Multifunction wide-band array design," , *IEEE Transactions on Antennas and Propagation*, vol. 47, no. 3, pp. 425–431, 1999.
- [3] H. Holter, T.-H. Chio, and D. H. Schaubert, "Experimental results of 144-element dual-polarized endfire tapered-slot phased arrays," *IEEE Transactions on Antennas and Propagation*, vol. 48, no. 11, pp. 1707–1718, 2000.
- [4] R. W. Kindt and W. R. Pickles, "All-Metal Flared-Notch Array Radiator for Ultrawideband Applications," *DTIC Document*, 2010.
- [5] J. J. Lee, R. Y. Loo, S. Livingston, V. I. Jones, J. B. Lewis, H. Yen, G. L. Tagonan, and M. Wechsberg, "Photonic wideband array antennas," *IEEE Transactions on Antennas and Propagation*, , vol. 43, no. 9, pp. 966–982, 1995.
- [6] J. J. Lee, S. Livingston, and R. Koenig, "A low-profile wide-band (5:1) dual-pol array," *IEEE Antennas and Wireless Propagation Letters*, vol. 2, no. 1, pp. 46–49, 2003.
- [7] J. J. Lee, S. Livingston, and R. Koenig, "Performance of a wideband (3-14 GHz) dual-pol array," in *Antennas and Propagation Society International Symposium*, 2004. IEEE, 2004, vol. 1, pp. 551–554.
- [8] J. G. Maloney, B. N. Baker, R. T. Lee, G. N. Kiesel, and J. J. Acree, "Wide scan, integrated printed circuit board, fragmented aperture array antennas," in *Antennas and Propagation (APSURSI), 2011 IEEE International Symposium on*, 2011, pp. 1965–1968.
- [9] M. Jones and J. Rawnick, "A new approach to broadband array design using tightly coupled elements," in *Military Communications Conference, 2007. MILCOM 2007*. IEEE, 2007, pp. 1–7.

- [10] W. F. Moulder, K. Sertel, and J. L. Volakis, "Superstrate-enhanced ultrawideband tightly coupled array with resistive FSS," *IEEE Transactions on Antennas and Propagation*, vol. 60, no. 9, pp. 4166–4172, Sep. 2012.
- [11] H. A. Wheeler, "Simple relation derived from a phased-array antenna made of an infinite current sheet," *IEEE Transactions on Antennas Propagation*, vol. 13, no. 4, pp. 506–514, 1965.
- [12] A. Neto and J. J. Lee, "'Infinite bandwidth' long slot array antenna," *IEEE Antennas and Wireless Propagation Letters*, vol. 4, no. 1, pp. 75–78, Dec. 2005.
- [13] J. Capmany and D. Novak, "Microwave photonics combines two worlds," *Nat. Photonics*, vol. 1, no. 6, pp. 319–330, 2007.
- [14] T. Miya, Y. Terunuma, T. Hosaka, and T. Miyashita, "Ultimate low-loss single-mode fibre at 1.55 μm ," *Electron. Lett.*, vol. 15, no. 4, pp. 106–108, 1979.
- [15] R. J. Mears, L. Reekie, I. M. Jauncey, and D. N. Payne, "Low-noise erbium-doped fibre amplifier operating at 1.54 μm ," *Electron. Lett.*, vol. 23, no. 19, pp. 1026–1028, 1987.
- [16] J. Macario, P. Yao, S. Shi, A. Zablocki, C. Harrity, R. D. Martin, C. A. Schuetz, and D. W. Prather, "Full spectrum millimeter-wave modulation," *Opt. Express*, vol. 20, no. 21, pp. 23623–23629, 2012.
- [17] X. Xie, Q. Zhou, K. Li, A. Beling, and J. C. Campbell, "High performance analog photonic link based on modified uni-traveling-carrier photodiode," in *2014 Conference on Lasers and Electro-Optics (CLEO)*, 2014, pp. 1–2.
- [18] Z. Yang, X. Xie, Q. Li, J. C. Campbell, and A. Beling, "20 GHz analog photonic link with 16 dB gain based on a high-power balanced photodiode," in *Photonics Conference (IPC), 2015*, 2015, pp. 144–145.
- [19] Z. Li, Y. Fu, M. Piels, H. Pan, A. Beling, J. E. Bowers, and J. C. Campbell, "High-power high-linearity flip-chip bonded modified uni-traveling carrier photodiode," *Opt. Express*, vol. 19, no. 26, pp. B385–B390, 2011.
- [20] J. Bai, S. Shi, G. J. Schneider, J. P. Wilson, Y. Zhang, W. Pan, and D. W. Prather, "Optically Driven Ultrawideband Phased Array With an Optical Interleaving Feed Network," *IEEE Antennas Wirel. Propag. Lett.*, vol. 13, pp. 47–50, 2014.

- [21] G. J. Schneider, J. A. Murakowski, C. A. Schuetz, S. Shi, and D. W. Prather, "Radiofrequency signal-generation system with over seven octaves of continuous tuning," *Nat. Photonics*, vol. 7, no. 2, pp. 118–122, 2013.
- [22] H. A. Wheeler, "The Radiation Resistance of an Antenna in an Infinite Array or Waveguide," *Proceedings of the IRE*, vol. 36, no. 4, pp. 478–487, Apr. 1948.
- [23] B. A. Munk, *Finite Antenna Arrays and FSS*, 1 edition. Piscataway, N.J.: Hoboken, N.J: Wiley-IEEE Press, 2003.
- [24] R. C. Hansen, "Linear connected arrays [coupled dipole arrays]," *IEEE Antennas and Wireless Propagation Letters*, vol. 3, no. 1, pp. 154–156, Dec. 2004.
- [25] E. A. Alwan, K. Sertel, and J. L. Volakis, "Circuit model based optimization of ultra-wideband arrays," in *2012 IEEE Antennas and Propagation Society International Symposium (APSURSI)*, 2012, pp. 1–2.
- [26] T. Durham, A. Jones, G. Gothard, and S. Ortiz, "Dual polarization antenna array with inter-element coupling and associated methods," US20070132643 A1, 14-Jun-2007.
- [27] J. A. Kasemodel, C.-C. Chen, and J. L. Volakis, "Wideband planar array with integrated feed and matching network for wide-angle scanning," *IEEE Transactions on Antennas and Propagation*, vol. 61, no. 9, pp. 4528–4537, Sep. 2013.
- [28] S. S. Holland and M. N. Vouvakis, "The planar ultrawideband modular antenna (PUMA) array," *IEEE Transactions on Antennas and Propagation*, vol. 60, no. 1, pp. 130–140, Jan. 2012.
- [29] I. Tzanidis, K. Sertel, and J. L. Volakis, "UWB low-profile tightly coupled dipole array with integrated balun and edge terminations," *IEEE Transactions on Antennas and Propagation*, vol. 61, no. 6, pp. 3017–3025, 2013.
- [30] S. March, "A Wideband Stripline Hybrid Ring (Correspondence)," *IEEE Transactions on Microwave Theory and Techniques*, vol. 16, no. 6, pp. 361–361, Jun. 1968.
- [31] J. A. Kasemodel, C. C. Chen, and J. L. Volakis, "Broadband planar wide-scan array employing tightly coupled elements and integrated balun," in *2010 IEEE International Symposium on Phased Array Systems and Technology (ARRAY)*, 2010, pp. 467–472.

- [32] J. A. Kasemodel, C. C. Chen, and J. L. Volakis, "Low-cost, planar and wideband phased array with integrated balun and matching network for wide-angle scanning," in *2010 IEEE Antennas and Propagation Society International Symposium (APSURSI)*, 2010, pp. 1–4.
- [33] Tengfei Xia, Shiwen Yang, and Zaiping Nie, "Design of a Tapered Balun for Broadband Arrays With Closely Spaced Elements," *IEEE Antennas and Wireless Propagation Letters*, vol. 8, pp. 1291–1294, 2009.
- [34] H. Ito, F. Nakajima, T. Furuta, and T. Ishibashi, "Continuous THz-wave generation using antenna-integrated uni-travelling-carrier photodiodes," *Semiconductor Science and Technology*, vol. 20, no. 7, pp. S191–S198, Jul. 2005.
- [35] K. Li, X. Xie, Q. Li, Y. Shen, M. E. Woodsen, Z. Yang, A. Beling, and J. C. Campbell, "High-Power Photodiode Integrated With Coplanar Patch Antenna for 60-GHz Applications," *IEEE Photonics Technology Letters*, vol. 27, no. 6, pp. 650–653, Mar. 2015.
- [36] S. Shi, J. Bai, R. Nelson, C. Schuetz, P. Yao, G. J. Schneider, Y. Zhang, D.W. Prather, "Ultrawideband Optically Fed Tightly Coupled Phased Array," in *Journal of Lightwave Technology*, vol. 33, no. 23, pp. 4781–4790, Dec.1, 1 2015.
- [37] X. Xie, Q. Zhou, K. Li, Y. Shen, Q. Li, Z. Yang, A. Beling, and J. C. Campbell, "Improved power conversion efficiency in high-performance photodiodes by flip-chip bonding on diamond," *Optica*, vol. 1, no. 6, p. 429, Dec. 2014.
- [38] X. Xie, K. Li, Y. Shen, Q. Li, J. Zang, A. Beling, and J. C. Campbell, "Photonic Generation of High-Power Pulsed Microwave Signals," *J. Lightwave Technol., JLT*, vol. 33, no. 18, pp. 3808–3814, Sep. 2015.
- [39] C. A. Balanis, *Antenna Theory: Analysis and Design, 3rd Edition*, 3 edition. Hoboken, NJ: Wiley-Interscience, 2005.
- [40] P. I. Deffenbaugh, R. C. Rumpf, and K. H. Church, "Broadband Microwave Frequency Characterization of 3-D Printed Materials," *IEEE Transactions on Components, Packaging and Manufacturing Technology*, vol. 3, no. 12, pp. 2147–2155, Dec. 2013.
- [41] R. Harrington and J. Mautz, "Theory of characteristic modes for conducting bodies," *IEEE Transactions on Antennas and Propagation*, vol. 19, no. 5, pp. 622–628, Sep. 1971.

- [42] J. Bai, "Optically addressed ultra-wideband phased antenna array," Thesis, University of Delaware, 2014.
- [43] B. Cantrell, J. Rao, G. Tavik, M. Dorsey, and V. Krichevsky, "Wideband array antenna concept," in *Radar Conference, 2005 IEEE International*, 2005, pp. 680–684.
- [44] D. D. Ross, M. R. Konkol, S. Shi and D. W. Prather, "Optically addressed ultra-wideband connected array antenna," *2016 International Workshop on Antenna Technology (iWAT)*, Cocoa Beach, FL, 2016, pp. 207-210.